Master thesis

Propagtion of blobs in NORTH

A study of NORTH Using Langmuir probes

Bjarke Brask Nielsen

Advisors: Peter Ditlevsen, Stefan Kragh Nielsen

Submitted: February 28, 2023

This thesis has been submitted to the The Faculty of Science, University of Copenhagen

Acknowledgements

I want to express my sincere gratitude to my supervisor at KU, Peter Ditlevsen and at DTU, Stefan Kragh Nielsen and Raheesty Devi Nem, for their unwavering support, guidance and encouragement throughout the entire process of writing this thesis. Their insightful feedback and expert knowledge have been invaluable to me, and their belief in my ability has given me the confidence to pursue my goals. I am truly grateful for their time and energy dedicated to helping me bring my research to life.

I would also like to thank my girlfriend, Emilie Wedenborg, for her unconditional love and support. She has been my source of strength and inspiration; her encouragement and motivation have been essential to my success. I am deeply thankful for her understanding and support, especially during the long hours and late nights spent writing this thesis.

Finally, I would like to express my gratitude to all those who have directly or indirectly contributed to the completion of this thesis. Their generosity, time, and effort have not gone unnoticed, and I am grateful for their support.

This thesis would not have been possible without the contributions of all those mentioned above, and for that, I am truly grateful.

Abstract

During this thesis, a Langmuir probe array consisting of multiple Langmuir probes was developed and tested at the plasma device NORTH located at Denmark's Technical University. The theory of Langmuir probes and drifts in general in plasma was explained in theory using the guiding centre plasma approximation for cold plasma and ended with a brief explanation of waves in cold plasma.

The probe array consisted of 12 independent Langmuir probes, each with circuitry designed to remove the bias signal and amplify the signal from the Langmuir probes. The circuitry was tested in a lab setting and found to work as intended for low frequencies, while the frequency response was worse than expected, likely due to a less-than-ideal choice of components for the circuitry. The new multi-probe array could measure more samples per second than possible before while allowing for measuring at multiple points in the plasma simultaneously.

A single Langmuir probe installed at NORTH was used to understand how the plasma behaves inside NORTH until the new multi-probe array was ready. The new multi-probe array was then used to measure the plasma density profile and temperature profile, as well as an investigation of blobs generated in the plasma. The measured plasma profiles agreed with earlier results at NORTH, and the measured velocity of blobs agreed with results from other papers. The blobs were found in 2 different regimes with a clear difference in velocities and shapes.

Contents

Chapter 1

Introduction

It is widely known that the increase in the well-being of all, historically, has led to larger energy needs[2]. Under the assumption that we will keep needing increasing amounts of energy, we need to find sustainable ways to produce this energy to reduce the toll we take on the climate[4]. One of the possible solutions is fusion-powered energy generation. This technology is being researched worldwide, with the most significant project being the ITER project[9], an international collaboration working to prove fusion as a viable energy source. One of the difficulties with fusion energy is containing and keeping the plasma within the device stable enough to produce more energy than it consumes by heating the device. To obtain fusion, the fuel (hydrogen/deuterium/tritium, most likely) must be heated to over 100 million degrees[5]. At these temperatures, the fuel ionises and becomes plasma. As the walls within the device can't sustain these temperatures, the plasma needs to be contained using strong magnetic fields.

The device being researched the most to do fusion power is the tokamak. A tokamak is a doughnut-shaped vacuum chamber in which the plasma is controlled using electromagnets. As plasma is electrically charged, it is hard to predict how it behaves in the device, which causes instabilities and loss of confinement due to turbulence and plasma drifts. At Denmark's Technical University, DTU, the device NORTH is located. NORTH is technically not a tokamak, as there isn't an induced current into the plasma; however, the plasma obtained is still helpful in better understanding plasma effects in tokamaks. This reduces the confinement of the devices, but it is still used to conduct plasma experiments. The device is being used to better understand plasma's physics, which is necessary for controlled fusion. The device NORTH is explained in detail in the following chapters.

To obtain a stable plasma, we need to understand the plasma and develop diagnostics able to measure the plasma. The theory of plasma physics in a tokamak is explained in chapter 2, while in chapter 3, diagnostics are being created and tested to measure in more detail than possible at the moment,

at the device NORTH. These new diagnostics are used to investigate plasma transport due to blobs in NORTH. Blobs are increases in charge densities of final size within the plasma.

I will take a prominent role in designing and building a probe system of Langmuir probes which will be tested at the Tokamak NORTH at DTU. This probe system will be used to measure the density and temperature of the plasma to a higher degree than before. The transport in the plasma's edge will be investigated and compared to the established results from other devices.

Chapter 2

Theory

From electromagnetism to plasma physics

A plasma is a collection of charged particles. The particles are to behave collectively, and the motion of these particles is controlled mainly by the electrodynamic forces[3]. One characteristic of plasma is the ability to "remove" local charge collections from the rest of the plasma. Suppose we consider a positively charged ball inserted into a plasma. In that case, electrons (or other negative particles) will surround this ball so that the potential difference between the ball and the main plasma can't be measured away from the ball. This sheath of electrons will have a size that we find by solving Poisson's equation in one dimension:

$$\epsilon_0 \nabla \phi = \epsilon \frac{d^2\phi}{dx^2} = -e(n_i - n_e) \tag{2.1}$$

For the case where the density of the positive ions is n_i, which in this case has an atomic number of $Z = 1$, the density of the negative particles (electrons) is n_e, and ϕ is the potential compared to the main plasma. Under the assumption that the mass of the electrons is much lower than the mass of the ions, we can assume the ions are not moving, as the electrons move much faster than the ions and therefore don't move significantly far enough in this timescale. This means the ion density is the same close to the ball as far away from the ball.

$$n_i = n_{inf} \tag{2.2}$$

Meanwhile, the electrons are distributed by the Maxwell-Boltzmann distribution:

$$f(v) = A\left(-\frac{E_e}{KT_e}\right) = A\left(-\frac{\frac{1}{2}mv^2 + q\phi}{KT_e}\right) \tag{2.3}$$

We find the electron density by integration:

$$n_e = \int_0^\infty A\left(-\frac{\frac{1}{2}mv^2 + q\phi}{KT_e}\right) dv =$$

$$\left[\frac{\sqrt{\pi}A(\sqrt{\frac{1}{2}}mv)}{2\sqrt{\frac{1}{2}}m}\left(\frac{e\phi}{KT_e}\right)\right]_0^\infty = \frac{\sqrt{\pi}}{2\sqrt{\frac{1}{2}}m}\left(\frac{e\phi}{KT_e}\right) =$$

$$n_\infty\left(\frac{e\phi}{KT_e}\right) \quad (2.4)$$

where we remember that $n_e = n_\infty$ when $\phi = 0$. substituting this into Poisson's equation, we have:

$$\epsilon_0\frac{d^2\phi}{dx^2} = en_\infty\left(exp\left(\frac{e\phi}{KT_e}\right) - 1\right) \quad (2.5)$$

If we Taylor expand this to the first order, it gives:

$$\frac{d^2\phi}{dx^2} = \frac{n_\infty e^2}{\epsilon_0 KT_e}\phi = \frac{\phi}{\lambda_D^2} \quad (2.6)$$

The solution to this is:

$$\phi = \phi_0 exp\left(-\frac{|x|}{\lambda_D}\right), \qquad \lambda_D = \sqrt{\frac{\epsilon_0 KT_e}{ne^2}} \quad (2.7)$$

The thickness of the sheath surrounding the ball is λ_D called the Debye length[3]. This gives the first criteria for plasma:

$$\lambda_D << L \quad (2.8)$$

Where L is the typical length scale of the plasma, this criterion says that the density of the plasma must be large enough compared to the temperature of the plasma so that the sheath thickness from local charge disturbances is small compared to the overall plasma size. At the same time, there must be enough particles inside the sheath to be seen as homogeneous. The number of particles inside a sphere with radius λ_D:

$$N_D = n\frac{4}{3}\lambda_D^3\pi \quad (2.9)$$

N_D is called the plasma parameter and is the second criterion for plasma. The last criterion, which is that electromagnetic forces rather than hydrodynamic forces must dominate, is:

$$\omega\tau > 1 \quad (2.10)$$

Where ω is the frequency for typical plasma oscillations, and τ is the mean time between collisions with neutral particles in the plasma.

Plasma physics

In plasma in a tokamak, you often have densities too large to find the dynamics of the plasma simply by solving Maxwell's equations, and you have too few particles for fluid dynamics to be a good approximation. The most comprehensive description of plasma is made from kinetic theory[17], though to get an idea of how the plasma behaves, we look at guiding centre plasma (GCP).

In GCP, we look at the single particle motions of ions and electrons subject to the Lorentz force to understand the motion the plasma undergoes inside NORTH.

Larmor gyration

To see where the name guiding centre comes from, we look at the case of a charged particle in a uniform magnetic field with no electric field. From the Lorentz force:

$$m\frac{dv}{dt} = q\bar{v} \times \bar{B} = q \begin{bmatrix} v_y B \\ -v_x B \\ 0 \end{bmatrix}, \qquad \bar{B} = B\hat{z} \qquad (2.11)$$

Differentiating again:

$$\frac{d^2v}{dt^2} = \frac{qB}{m} \begin{bmatrix} \frac{dv_y}{dt} \\ -\frac{dv_x}{dt} \\ 0 \end{bmatrix} = -\left(\frac{qB}{m}\right)^2 \begin{bmatrix} v_x \\ v_y \\ 0 \end{bmatrix} \qquad (2.12)$$

This is simply a harmonic motion with the cyclotron frequency:

$$\omega_c \equiv \frac{|q|B}{m} \qquad (2.13)$$

The orbit is clockwise for positive ions and counterclockwise for negative ions or electrons. The guiding centre is the centre at which the particle is orbiting around. The radius of the orbit is called the Larmor radius:

$$r_L \equiv \frac{v_\perp}{\omega_c} \qquad (2.14)$$

This is also an example of how particles follow the magnetic lines, lines drawn following the magnetic field with constant size, as the velocity perpendicular to the magnetic field is used in the orbit around the guiding centre. In contrast, any velocity in $\hat{z}$, along the magnetic field, is conserved.
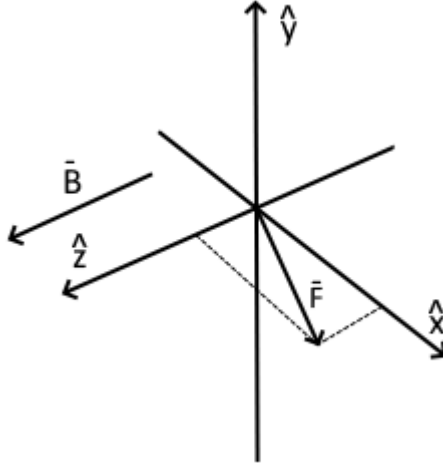
Figure 2.1: External force $\bar{F}$ in the $\hat{x}$-$\hat{z}$ plane.

General drift due to an external force

If we imagine an arbitrary constant force acting on the particle, we have:

$$m\frac{dv}{dt} = q\bar{v} \times \bar{B} + \bar{F}, \qquad \bar{B} = B\hat{z}, \ \ \bar{F} = F_x\hat{x} + F_z\hat{z} \qquad (2.15)$$

See figure 2.1 for a sketch of coordinates.

The $\hat{z}$ component is simply an acceleration in the same direction as the magnetic field, $\bar{B}$:

$$\frac{dv_z}{dt} = \frac{F_z}{m} \rightarrow v_z = \frac{F_z}{m}t + v_{z0} \qquad (2.16)$$

Where v_{z0} is the starting velocity in the $\hat{z}$ direction.

Looking only at the transverse components, we differentiate as before:

$$\frac{d^2v}{dt^2} = \omega_c \begin{bmatrix} \frac{dv_y}{dt} \\ -\frac{dv_x}{dt} \end{bmatrix} = -\omega_c^2 \begin{bmatrix} v_x \\ v_y + \frac{F_x}{qB} \end{bmatrix} \qquad (2.17)$$

This motion is again the Larmor gyration, but a drift of the guiding centre is superimposed, a drift along the magnetic field, and a drift perpendicular to the magnetic field. To get an equation for the drift, we find the solution to the static equation, as the acceleration ($m\frac{dv}{dt}$) is only responsible for the Larmor gyration, which we already know of.

$$0 = \frac{\bar{F}}{q} + \bar{v} \times \bar{B} \qquad (2.18)$$

Taking the cross product on each side and solving the triple vector prod-

uct using the BAC rule[1]:

$$0 = \frac{\bar{F}}{q} + \bar{v} \times \bar{B} = \frac{\bar{F}}{q} \times \bar{B} - \bar{B} \times (\bar{v} \times \bar{B}) = \frac{\bar{F}}{q} \times \bar{B} - \bar{v}B^2 + \bar{B}(\bar{v} \cdot \bar{B}) =$$

$$\frac{\bar{F}}{q} \times \bar{B} - \bar{v}B^2 + \bar{B}(v_{\parallel}B) = \frac{\bar{F}}{q} \times \bar{B} - \bar{v}B^2 + \bar{v}_{\parallel}B^2 = \frac{\bar{F}}{q} \times \bar{B} - B^2(\bar{v} - \bar{v}_{\parallel}) =$$

$$\frac{\bar{F}}{q} \times \bar{B} - B^2 v_{\perp gc}^- = 0 \quad (2.19)$$

From this, we define the guiding centre drift arising from a force acting upon the particle as:

$$v_F \equiv v_{\perp gc}^- = \frac{\bar{F} \times \bar{B}}{qB^2} \quad (2.20)$$

This means that, in total, a charged particle under a constant force in a magnetic field has:

1. A linear acceleration along the magnetic field.

2. Larmor gyration perpendicular to the magnetic field.

3. A drift of the guiding centre perpendicular to the force and the magnetic field.

Drift due to magnetic gradient

A gradient in the magnetic field means that the particle experiences a variable force from the Lorentz force due to being in a different position where the magnetic field is different in the gyration. To find the drift arising from this, we find the average force exerted on the particle from the loop. If the B field points in the $\hat{z}$ direction, and the gradient of the magnetic field points in the $\hat{y}$ direction, the force in the $\hat{y}$ direction on the particle are:

$$F_y = q\bar{v} \times \bar{B}(y) = -qv_x B(y) \quad (2.21)$$

From before, we know the Larmor motion is harmonic, so we can let $v_x = v_{\perp}cos(\omega_c t)$, which then means we have to have $v_y = \hat{q}v_{\perp}sin(\omega_c t)$. We Taylor-expand the magnetic field around the guiding centre:

$$B(y) = B_0 + (y - y_0)\frac{dB}{dy} = B_0 + \hat{q}\frac{v_{\perp}}{\omega_c}cos(\omega_c t)\frac{dB}{dy} = B_0 + \hat{q}r_L cos(\omega_c t)\frac{dB}{dy} \quad (2.22)$$

This gives the Lorentz force:

$$F_y = -qv_x B(y) = -q\left(v_{\perp}cos(\omega_c t)\right)\left(B_0 + \hat{q}r_L cos(\omega_c t)\frac{dB}{dy}\right)$$

$$= -qv_{\perp}\left(B_0 cos(\omega_c t) + \hat{q}r_L cos^2(\omega_c t)\frac{dB}{dy}\right) \quad (2.23)$$

---

[1] $a \times (b \times c) = b(a \cdot c) - c(a \cdot b)$

Averaging this over one gyration, the first term in the parenthesis gives zero, while the second term gives a factor of $\frac{1}{2}$ from the squared cosine;

$$\langle F_y \rangle = -\frac{1}{2} q \hat{q} v_\perp r_L \frac{dB}{dy} \tag{2.24}$$

Since the choice of y-axis was arbitrary, we can generalize the expansion in the magnetic field as $\bar{B} = \bar{B}_0 + (\bar{r} \cdot \nabla)\bar{B}$, from where we then get:

$$\langle \bar{F} \rangle = -\frac{1}{2} q \hat{q} v_\perp (\bar{r} \cdot \nabla)\bar{B} = -\frac{1}{2} q \hat{q} v_\perp r_L \nabla \bar{B} \tag{2.25}$$

As we now have the force, we can find the corresponding drift:

$$v_{\nabla B} = \frac{\bar{F} \times \bar{B}}{qB^2} = -\frac{q \hat{q} v_\perp r_L}{qB^2} (\nabla \bar{B} \times \bar{B}) = \frac{\hat{q} v_\perp r_L}{B^2} \bar{B} \times \nabla \bar{B} \tag{2.26}$$

This means that in our situation, as described above, we get a drift in the $\hat{x}$ direction, where the sign depends on the charge.

As the plasma device is spherical, a drift will also arrive from the centrifugal force acting on the particles. The centrifugal force is $F_{cen} = \frac{mv_\parallel^2}{R}\hat{r}$, where R is the radius of the orbit in the tokamak along the B field, and $\hat{r}$ is the direction of the said vector. This gives a drift which adds to the gradient drift, as the forces have the same direction.

In NORTH, a magnetic field is created by the eight coils around the torus. This creates a magnetic field which runs around the torus on the inside. As there is a higher density of coils close to the centre of the torus compared to the outside, the magnetic field is strongest closer to the centre; therefore, we have a magnetic field gradient that points inward to the centre of the torus.

A sketch of the cross-section of the device is seen in figure 2.2 together with the drift of the particles. As the gradient is in the direction $\hat{r}$ direction, while the B field is into the sketch, we have a gradient and curvature drift that points upward for positive ions and downward for electrons. This gives rise to an electric field pointing downwards. This electric field results in a new drift from the Lorentz force from this electric field, $\bar{F} = -qE\hat{z}$:

$$v_E = -\frac{q}{q} \frac{\bar{E} \times \bar{B}}{B^2} = \frac{E}{B}\hat{r} \tag{2.27}$$

This means all charged particles in the plasma drift towards the edge of the plasma device, no matter the sign of the charge. This gives rise to loss of confinement for the plasma.

Filament transport - Blobs

Local density perturbations in the plasma, called blobs, are also influenced by the drifts mentioned above. Blobs are found to travel radially outwards
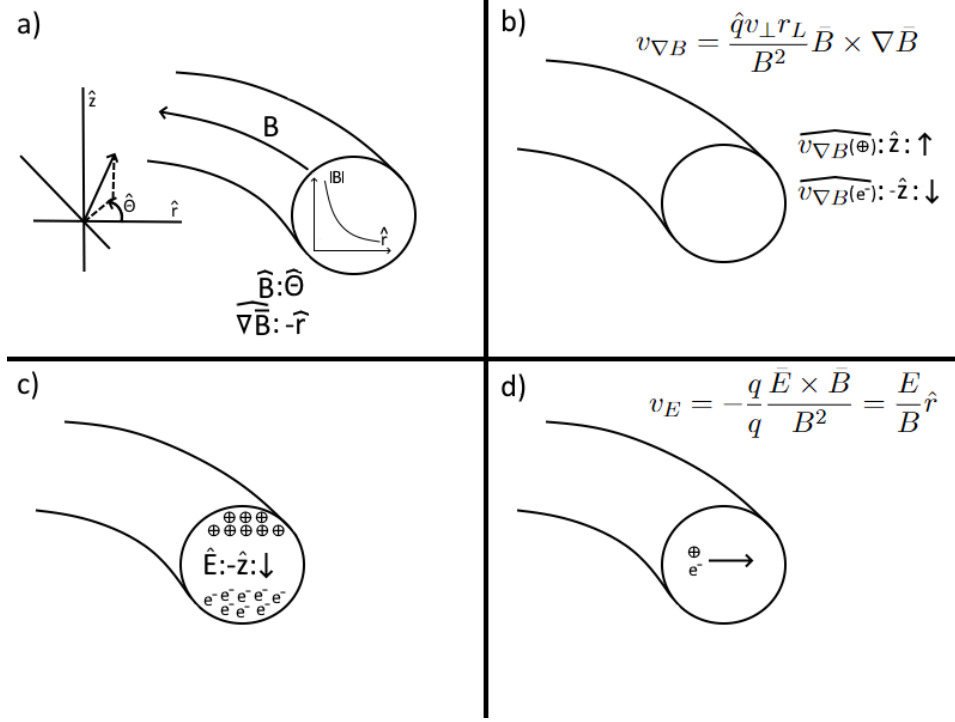
Figure 2.2: a) Sketch of the cylindrical coordinate system and the direction of the magnetic and its gradient. b) due to the gradient drift, ions drift upwards while electrons drift downwards. c) The drifted particles generate an electric field pointing downwards. d) The drift arising from the electric field drifts all charged particles outwards of the machine.

with a velocity of up to one-tenth of the ion sound speed[10]. Under the assumption of cold ions, the sound speed is calculated as follows:

$$v_s = \frac{\gamma_e Z T_{eV}}{M}$$

Where $\gamma_e \sim 1$, Z is the atomic charge number, M is the mass of the ion forming the plasma, while T_{eV} is the plasma temperature. If we assume the temperature of the plasma to be $8eV$, we find an acoustic velocity of:

$$v_s^H = 28\frac{km}{s} \tag{2.28}$$

For hydrogen, and:

$$v_s^{He} = 20\frac{km}{s} \tag{2.29}$$

for Helium.

The dynamics of blobs have been investigated numerically by different people and are shown to have complex behaviour. In appendix D in figure

9

D.1, made by A.E. Thrysøe, seeded blobs are simulated, and we can see the evolution of these blobs as they propagate outwards. As we can see in the figure, the shape of the blobs are very different depending on where in the tokamak the blob is measured, i.e. it might be thinning over time if we measure the blob at $y = 0mm$ and it might be thickening if we measure the blob at $y = -10mm$. In appendix D figure D.2, from [7], blobs are both simulated and measured from ESEL[15] and TCV[6] respectively. These blobs are shown to have a profile where the blobs have a sharp rise and a longer tail. We hope to be able to detect blobs in NORTH which has some of these characteristics.

Langmuir probe

We will be using Langmuir probes to measure the parameters of the plasma.

A Langmuir probe is a thin piece of wire inserted into the plasma. When a bias potential is applied to the probe, which differs from the plasma potential, the probe collects either ions or electrons due to the difference in potential. When a potential lower than the plasma potential is applied, primarily ions are collected, though fast electrons might still be collected. Only ions are collected if the applied bias potential is much lower than the plasma potential. And the opposite is true for bias potentials higher than the plasma potential. To find the current flowing to the probe at different bias potentials, we use Poisson's equation to find the minimum particle velocity required to reach the probe so that we can relate the current flowing to the probe to the density and temperature of the plasma.

When applying a large negative bias potential, the plasma creates a sheath surrounding it, masking the potential drop from the rest of the plasma. We imagine the situation in figure 2.3, where ions enter the sheath, at $x = 0$, with a drift velocity of u_0. The ions must have a drift velocity towards the probe so that the loss of ions to the probe compared to the regions of the plasma where they were created by ionization are balanced. We assume the temperature of the ions to be zero; $T_i = 0$ so that all ions enter the sheath with speed u_0.

By conservation of energy, we have:

$$\frac{1}{2}Mu(x)^2 = \frac{1}{2}Mu_0^2 - e\phi(x) \tag{2.30}$$

$u(x)$ is the velocity of the ions inside the sheath, and $-e\phi(x)$ is the energy from the potential. This gives:

$$u(x) = \sqrt{u_0^2 - \frac{2e\phi(x)}{M}} \tag{2.31}$$

From the continuity equation, for ions, we have that $n_{00} = n_i(x)(x)$, where $n_i(x)$ is the density of ions in the sheath and n_0 is the density of the
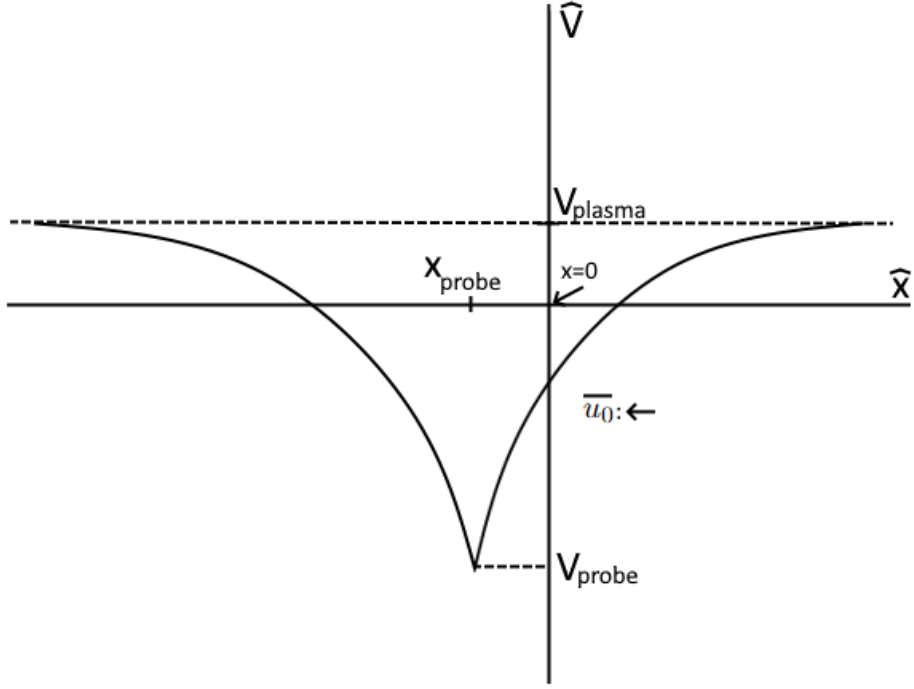
Figure 2.3: A sketch of the sheath potential around a negative probe.

main plasma. Combining this with the velocity above, we have:

$$n_i(x) = n_0 \sqrt{1 - \frac{2e\phi(x)}{Mu_0^2}} \qquad (2.32)$$

Assuming steady-state, the electrons are distributed with the Boltzmann relation[3]

$$n_e(x) = n_0 e^{\frac{e\phi}{KT_e}}, \qquad (2.33)$$

This now means Poisson's equation gives:

$$\epsilon_0 \frac{d^2\phi(x)}{dx^2} = e(n_e(x) - n_i(x)) = e\left(n_0 e^{\frac{e\phi}{KT_e}} - n_0\sqrt{1 - \frac{2e\phi(x)}{Mu_0^2}}\right) \qquad (2.34)$$

To simplify the expression, we rewrite the expression into the following dimensionless quantities: E_p as the potential energy in terms of thermal energy, L as the length in terms of Debye length, and U as the velocity of the particle in terms of the thermal velocity:

$$E_p \equiv -\frac{e\phi(x)}{KT_e} \qquad (2.35)$$

11

$$L \equiv x \sqrt{\frac{n_0 e^2}{\epsilon_0 K T_e}} \tag{2.36}$$

$$U \equiv \frac{u_0}{\sqrt{K T_e / M}} \tag{2.37}$$

so that we have

$$E_p'' = \left(1 + \frac{2E_p}{U^2}\right)^{-\frac{1}{2}} - e^{-E_p} \tag{2.38}$$

Where E_p is differentiated with respect to L

We then multiply both sides with E_p', after which we integrate from 0 to L:

$$\int_0^L E_p' E_p'' dL_1 = \int_0^L E_p' \left(1 + \frac{2E_p}{U^2}\right)^{-\frac{1}{2}} dL_1 - \int_0^L E_p' e^{-E_p} dL_1 \tag{2.39}$$

Since E_p is the potential scaled, and L is the distance from the sheath edge scaled, we have that $E_p = 0$ when $L = 0$ when we define that the potential is zero in the central plasma.

We are now able to complete the integrations:

$$\int_0^L E_p' E_p'' dL_1 = [E_p' E_p']_0^L - \int_0^L E_p'' E_p' dL_1 \rightarrow \int_0^L E_p' E_p'' dL_1 =$$
$$\frac{1}{2}[E_p' E_p']_0^L = \frac{1}{2}(E_p'^2 - E_p'(0)^2) \tag{2.40}$$

$$\int_0^L E_p' \left(1 + \frac{2E_p}{U^2}\right)^{-\frac{1}{2}} dL_1 = \int_0^{L_u} u^{-\frac{1}{2}} E_p' \frac{U^2}{2E_p'} du = [U^2 u^{\frac{1}{2}}]_0^{L_u} =$$
$$\left[U^2 (1 + \frac{2E_p}{U^2})\right]_0^L = U^2 \left(\sqrt{1 + \frac{2E_p}{U^2}} - 1\right) \tag{2.41}$$

$$\int_0^L e^{-E_p} E_p' dL_1 = [e^{-E_p}]_0^L = e^{-E_p} - 1 \tag{2.42}$$

With the assumption $\mathbf{E} = 0$ inside the plasma, we have $E_p(0)' = 0$, so that:

$$\frac{1}{2} E_p'^2 = U^2 \left(\sqrt{1 + \frac{2E_p}{U^2}} - 1\right) + e^{-E_p} - 1 \tag{2.43}$$

Since $E_p'^2$ is positive, the right-hand side must be positive at all values of E_p. Regarding the sheath edge (low E_p), we can Taylor-expand the right-hand side to get (ignoring E_p terms of order higher than 2):

$$U^2 < 1 \rightarrow u_0 > \sqrt{\frac{K T_e}{M}} \tag{2.44}$$

Which says that ions must enter the sheath with a velocity of $\sqrt{\frac{KT_e}{M}}$. This is known as the *Bohm sheath criterion*[16].

We can now use this velocity to determine ion density at the sheath edge. We start by redefining the potential so that the potential at the sheath edge is $-\frac{1}{2}KT_e/e$. This gives a pre-sheath potential[12] of $\frac{1}{2}KT_e/e$ so that the ions have the velocity found above. If the electrons are Maxwell-Boltzmann distributed, we can find n_s:

$$n_s = n_0 e^{e\phi_s/KT_e} = n_0 e^{-\frac{1}{2}} \approx 0.61 n_0 \approx \frac{1}{2} n_0 \qquad (2.45)$$

We can now determine what the current flowing to the probe, at large negative bias voltages, is:

$$I_{is} = e n_s \langle u \rangle_{thermal} A_p = \frac{1}{2} n_0 e A_p \sqrt{\frac{KT_e}{M}} \qquad (2.46)$$

This is called the ion saturation current. A_p is the collection area of the probe, which often is just above the surface area of the probe. We can use this to determine the density of the plasma when we find the temperature of the plasma.

When the bias voltage isn't very negative, electrons are also collected. In an ideal planar probe, the electrons collected before the plasma potential is met are exponential (assuming a maxwell-Boltzmann distribution of the electrons) and saturate at an electron saturation current when the bias potential is larger than the plasma potential, and all electrons are collected. The current density to the probe from electrons is:

$$
\begin{aligned}
j_e(V_B) &= q \int v_x n_e \left(\frac{m_e}{2\pi KT_e} \right)^{\frac{3}{2}} e^{-\frac{m_e v^2}{2KT_e}} dv \\
&= e n_e \sqrt{\frac{m_e}{2\pi KT_e}} \int_{v_{min}}^{\infty} v_x e^{-\frac{m_e v_x^2}{2KT_e}} dv_x \qquad (2.47) \\
&= e n_e \sqrt{\frac{KT_e}{2\pi m_e}} e^{-\frac{e(V_p - V_B)}{T_e}}
\end{aligned}
$$

Where $v_m in$ is the minimum energy required for the electrons to overcome the potential $V_P - V_B$, the relative probe potential. This is found by the conservation of energy:

$$\frac{1}{2} m_e v_{min}^2 = e(V_p - V_B) \rightarrow v_{min} = \sqrt{\frac{2e(V_p - V_B)}{m_e}} \qquad (2.48)$$

If the bias potential is larger than the plasma potential, the electron current density saturates so that we have:

$$j_e(V_B) = e n_e \sqrt{\frac{KT_e}{2\pi m_e}} e^{-\frac{e(V_p - V_B)}{T_e}}, \qquad for \ V_B < V_p \qquad (2.49)$$

$$j_e(V_B) = en_e\sqrt{\frac{KT_e}{2\pi m_e}}, \qquad for \ V_B >= V_p \qquad (2.50)$$

We find the electron current by multiplying with the area of the probe:

$$I_e = I_{es}e^{-\frac{e(V_p - V_B)}{T_e}}, \qquad for \ V_B < V_p \qquad (2.51)$$

$$I_e = I_{es}, \qquad for \ V_B >= V_p \qquad (2.52)$$

$$I_{es} = en_e A_p\sqrt{\frac{KT_e}{2\pi m_e}} \qquad (2.53)$$

With this, we can find the current flowing to the probe:

$$\begin{aligned}
I &= I_i + I_e \\
I &= I_{es}e^{-\frac{e(V_p - V_B)}{KT_e}} + I_{is}, \qquad for \ V_B < V_p \quad (2.54) \\
I &= I_{es}, \qquad\qquad\qquad\qquad for \ V_B >= V_p
\end{aligned}$$

As derived above, a sketch of an ideal planar Langmuir probe is seen in figure 2.4. Measuring the current flowing to the probe at different bias voltages lets us find the plasma density using the current at large negative bias, the plasma's temperature using the exponential part's slope, and the floating potential by the point at which the measured current is zero.

Since the Langmuir probe used is cylindrical instead of planar, edge effects result in the IV curve being less well-defined since the collection area of the probe increases as the voltage difference between the probe and ground increases. This increase in collection area results in the IV curve looking more smooth and not plateauing compared to the ideal planar probe.

In practice, we use cylindrical probes, introducing boundary conditions to the probe. This gives rise to a sheath with a larger surface than the surface of the probe. Langmuir and Mott-Smith[13] derived this effect, which is mainly seen as an approximately linear increase of the electron saturation current and rounding the "knee" where we go from exponential to linear. This makes it hard to determine the electron saturation current. But, as we aren't going to measure this in this project, we aren't delving further into this. A general sketch of the IV curve for a cylindrical Langmuir probe is seen in figure 2.5.

Plasma waves and heating in NORTH

While GCP is great for getting a general idea of how particles in a plasma behave, we introduce plasma waves to gain a deeper understanding of the
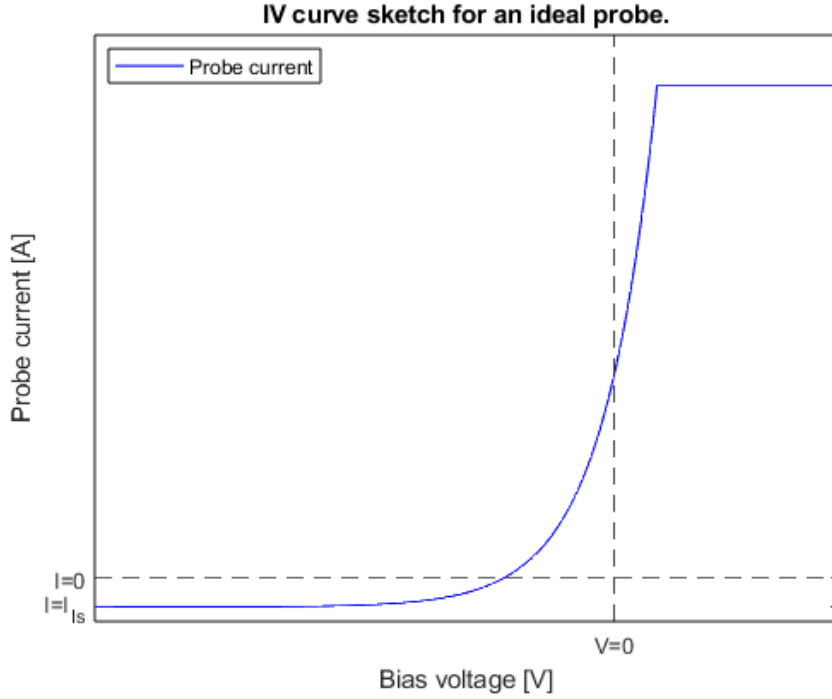
Figure 2.4: A sketch showing the general shape of the current-voltage curve (I-V curve) using an ideal planar probe.

behaviour of plasma and how the plasma in NORTH is heated. In general, both electrostatic and electromagnetic waves can propagate inside a plasma. We look again at the limit of cold plasma, i.e., ions don't move.

To start, we use Maxwell's equations together with the equation of motion for a particle in an electromagnetic field:

$$\nabla \times \bar{E} = -\frac{\partial \bar{B}}{\partial t} \tag{2.55}$$

$$\nabla \times \bar{B} = \mu_0(\bar{j} + \epsilon_0 \frac{\partial \bar{E}}{\partial t}) \tag{2.56}$$

$$m\frac{d\bar{v}}{dt} = q(\bar{E} + \bar{v} \times \bar{B}) \tag{2.57}$$

If we assume that the waves in the plasma are small perturbations to the main electromagnetic field, we can assume that:

$$\bar{E} = \bar{E}_0 + \bar{E}_1 e^{i(\bar{k}\bar{r}-wt)} = \bar{E}_1 e^{i(\bar{k}\bar{r}-wt)} \tag{2.58}$$

$$\bar{B} = \bar{B}_0 + \bar{B}_1 e^{i(\bar{k}\bar{r}-wt)} \tag{2.59}$$

15

IV curve sketch for an ideal cylindrical probe.
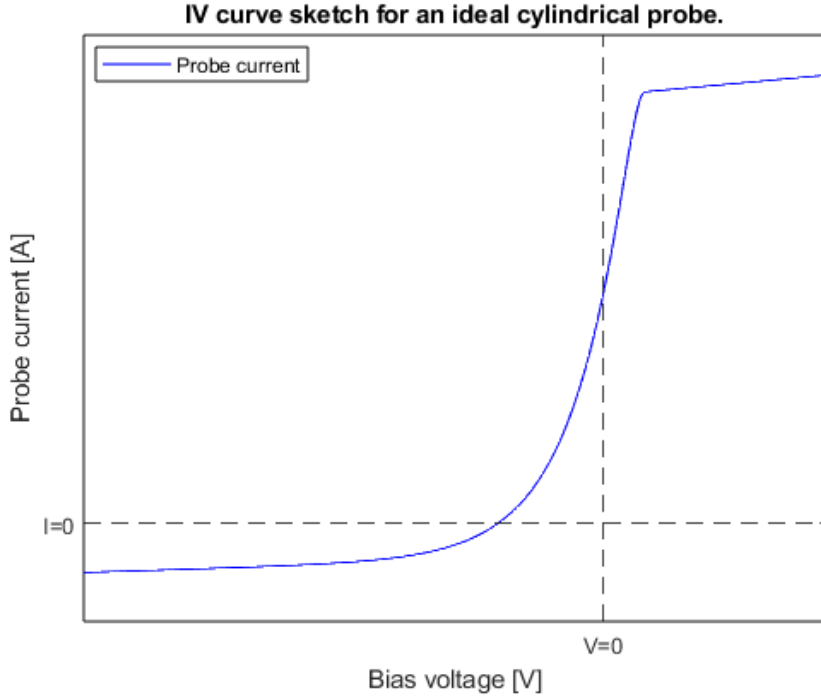
Figure 2.5: A sketch of the IV curve of a cylindrical Langmuir curve.

$$\bar{v} = \bar{v}_0 + \bar{v}_1 e^{i(\bar{k}r - wt)} = \bar{v}_1 e^{i(\bar{k}r - wt)} \tag{2.60}$$

Since we still assume that the plasma is neutral, the static electric field $\bar{E}_0$ is zero. $\bar{B}_0$ is the static magnetic field. We also move the frame of reference so that any constant velocity, $\bar{v}_0$, is zero.

If we combine these equations and linearize them, assuming that the perturbation is small, we can find a wave equation for waves in a cold plasma. This is relevant since the plasma in the device NORTH is heated using waves in plasma. Depending on the angles between the wave vector $\bar{k}$, electric field $\bar{E}_1$ and the magnetic field $\bar{B}_0$, the wave equation gives many different waves, which have different cut-offs and resonances. In the following, I'll only show a derivation in the case of the ordinary wave called O-waves, but the derivation of the different waves can be found in *Plasma Waves* by D. G. Swanson[17].

The O-wave is a wave which propagates perpendicular to the static magnetic field and has the electric field component along the static magnetic field. We place the frame of reference so that $\hat{B}_0 = \hat{E}_1 = \hat{z}$ and $\hat{k} = \hat{x}$.

We start by taking the curl of equation 2.55:

$$\nabla \times \left(\nabla \times \bar{E} \right) = \nabla \times \left(-\frac{\partial \bar{B}}{\partial t} \right) = -\frac{\partial}{\partial t} \left(\nabla \times \bar{B} \right) \tag{2.61}$$

16

We then insert equation 2.56:

$$\nabla \times \left(\nabla \times \bar{E} \right) = -\frac{\partial}{\partial t} \left(\mu_0 \left(\bar{j} + \epsilon_0 \right) \frac{\partial \bar{E}}{\partial t} \right) = -\mu_0 \left(\frac{\partial \bar{j}}{\partial t} + \epsilon_0 \frac{\partial^2 \bar{E}}{\partial t^2} \right) \quad (2.62)$$

Since $\bar{j} = qn\bar{v}$:

$$\bar{j} = qn\bar{v}_1 e^{i(\bar{k}\bar{r} - \omega t)} \quad (2.63)$$

Which we insert in equation 2.62, and calculate the derivative:

$$\nabla \times \left(\nabla \times \bar{E}_1 \right) = -\mu_0 \left(-i\omega qn\bar{v}_1 - \epsilon_0 \omega^2 \bar{E}_1 \right) \quad (2.64)$$

Calculating the left-hand side:

$$\nabla \times \left(\nabla \times \bar{E}_1 \right) = \nabla \left(\nabla \cdot \bar{E}_1 \right) - \nabla^2 \bar{E}_1 = -\bar{k} \left(\bar{k} \cdot \bar{E}_1 \right) + k^2 \bar{E}_1 \quad (2.65)$$

Since $\hat{k}$ is perpendicular on $\hat{E}_1$, we have:

$$k^2 \bar{E}_1 = \mu_0 \left(i\omega qn\bar{v}_1 + \epsilon_0 \omega^2 \bar{E}_1 \right) \quad (2.66)$$

We find another relation between $\bar{E}_1$ and $\bar{v}_1$ using equation 2.57:

$$m\frac{d\bar{v}}{dt} = -im\omega\bar{v} = q\left(\bar{E} + \bar{v} \times \bar{B} \right) \quad (2.67)$$

Linearizing $\bar{v} \times \bar{B} \rightarrow \bar{v}_1 \times \bar{B}_0$, gives us:

$$-i\omega m\bar{v}_1 = q\bar{E}_1 + q\bar{v}_1 \times \bar{B}_0 = q\bar{E}_1 \quad (2.68)$$

$$\bar{v}_1 = \frac{-q\bar{E}_1}{i\omega m} \quad (2.69)$$

Substituting into equation 2.66, we find the dispersion relation:

$$k^2 \bar{E}_1 = \mu_0 \left(i\omega qn \frac{-q\bar{E}_1}{-i\omega m} + \epsilon_0 \omega^2 \bar{E}_1 \right) \quad (2.70)$$

$$\omega^2 = c^2 k^2 - \omega_p^2 \quad (2.71)$$

Where $\omega_p^2 = \frac{e^2 n}{m\epsilon_0}$ is the plasma frequency. This wave is the O-wave, which has the most straightforward dispersion relation. From this, we can see that the wave can't propagate when ω is below ω_p as k is then purely imaginary. The point at which $k = 0$ is the cut-off frequency and is the frequency at which the wave is reflected.

Plasma heating in NORTH

NORTH is primarily heated using O-waves, made by a microwave source with a frequency of $f_h = 2.45GHz$. The electrons in the plasma absorb waves at the electron cyclotron resonance $\omega_{ce} = \frac{eB}{m_e}$. Since there is a substantial amount of neutral gas inside NORTH, the electrons then ionize nearby gas, generating more plasma and increasing the plasma density. To figure out what the magnetic field in NORTH looks like, we can use Amperes law around the torus through the toroidal field coils:

$$\oint \bar{B} \cdot d\bar{l} = \mu I_{enclosed} \tag{2.72}$$

Due to symmetry, the line integral is simply the circumference of a circle at a radius r times the magnetic field since the magnetic field is constant at the same r. The current enclosed in radius r is the current through the coils, times the number of turns, N, through radius r:

$$\oint \bar{B} \cdot d\bar{l} = 2\pi r B = \mu I_{enclosed} = \mu_0 I_{coil} N \tag{2.73}$$

$$B = \frac{\mu_0 N I_{coil}}{2\pi r} \tag{2.74}$$

Where we assume $\mu \sim \mu_0$.

NORTH has eight coils, each with 12 turns, which means $N = 96$. If we assume the current through the coils is $I_{coil} = 1000A$, we can find the position in NORTH at which the electron cyclotron resonance is:

$$2\pi r B = \mu_0 I_{coil} N \rightarrow r = \frac{1}{B}\frac{\mu_0 N I_{coil}}{2\pi} = \frac{e}{\omega_{ce} m_e}\frac{\mu_0 N I_{coil}}{2\pi} = \frac{\mu_0 N I_{coil} e}{4\pi^2 m_e f_h} \tag{2.75}$$

Inserting the values assumed above, the magnetic field and the resonance can be seen in figure 2.6.

From this, the plasma is heated at a radius of $22cm$. If we want to heat the plasma with O-waves, the wave has to travel through the plasma until it reaches the electron cyclotron resonance. If the O-wave reaches plasma with a too high plasma frequency, i.e. the density is too large, it is reflected and won't heat the plasma. As we heat with a source at $2.45GHz$, we can calculate the density at which O-waves are reflected:

$$\omega_h^2 = \frac{e^2 n}{m_e \epsilon_0} \rightarrow n = \frac{m\epsilon_0 \omega_h^2}{e^2} = 7.4 \times 10^{16} m^{-3} \tag{2.76}$$

This means that using solely O-waves, we won't heat the plasma from the LFS unless it has a density lower than $7.4 \times 10^{16} m^{-3}$. Plasma in which the density is too high to be heated using O-Waves is called over-dense.
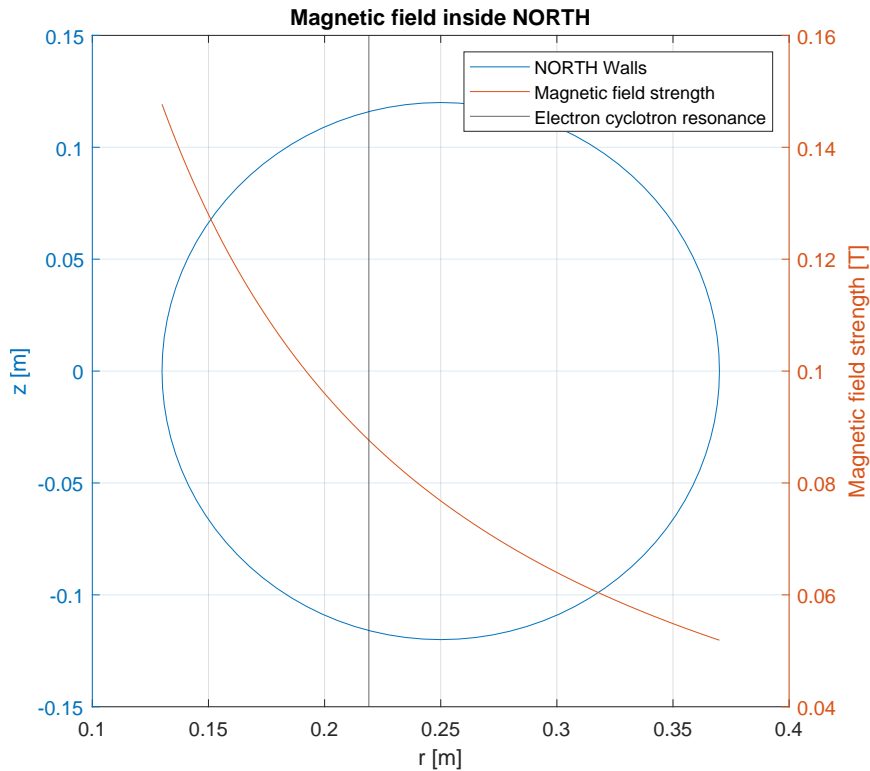
Figure 2.6: A plot of the magnetic field inside NORTH. The blue plot shows the cross-section of NORTH, while the orange plot shows the strength of the magnetic field depending on the distance to the centre of NORTH. The grey line shows the radius at which the electron cyclotron resonance is located, $r_{heating} = 22cm$.

OXB heating

One way to heat over-dense plasma is through OXB heating. When solving equations 2.55 through 2.57 where the wave isn't required to propagate perpendicular to the static magnetic field, and the electric field can have components in any direction, we end up with different waves, which has different cut-offs and resonances.

One possibility is the extraordinary wave, $X - wave$. It has a more complex dispersion relation than the $O - wave$ and has multiple cut-offs and resonances[17].

If the angle between the magnetic field and the $O - wave$ is close to the right angle[11] (This angle depends on the plasma), the $O - wave$ couples to the $X - wave$ at the $O - wave$ cut-off, so that the $O - wave$ can be converted to a $X - wave$ at the reflection. The microwave source at NORTH is angled to make this possible. This $X - wave$ then has a resonance at the

upper hybrid resonance, at which the $X - wave$ converts into an electron Bernstein wave, EBW. The EBW doesn't have cut-offs and can propagate through the plasma until it reaches the electron cyclotron resonance and heats the plasma. As the EBW doesn't have cut-offs, it is possible to heat over dense plasma using this OXB heating. It isn't clear if the plasma is heated with/partly with OXB heating at NORTH yet, but the device is set up for it to be possible.

To get an understanding of the OXB heating, I have drawn a CMA diagram[2] at figure 2.7. The cut-offs and resonances of the $O - wave$ and $X - wave$ are drawn at this, as well as the possible heating schemes at NORTH. The $X - wave$ has a cut-off at the L and R cut-offs. To see the complete CMA diagram, see appendix C.

---

[2]Clemmow– Mullaly–Allis diagram
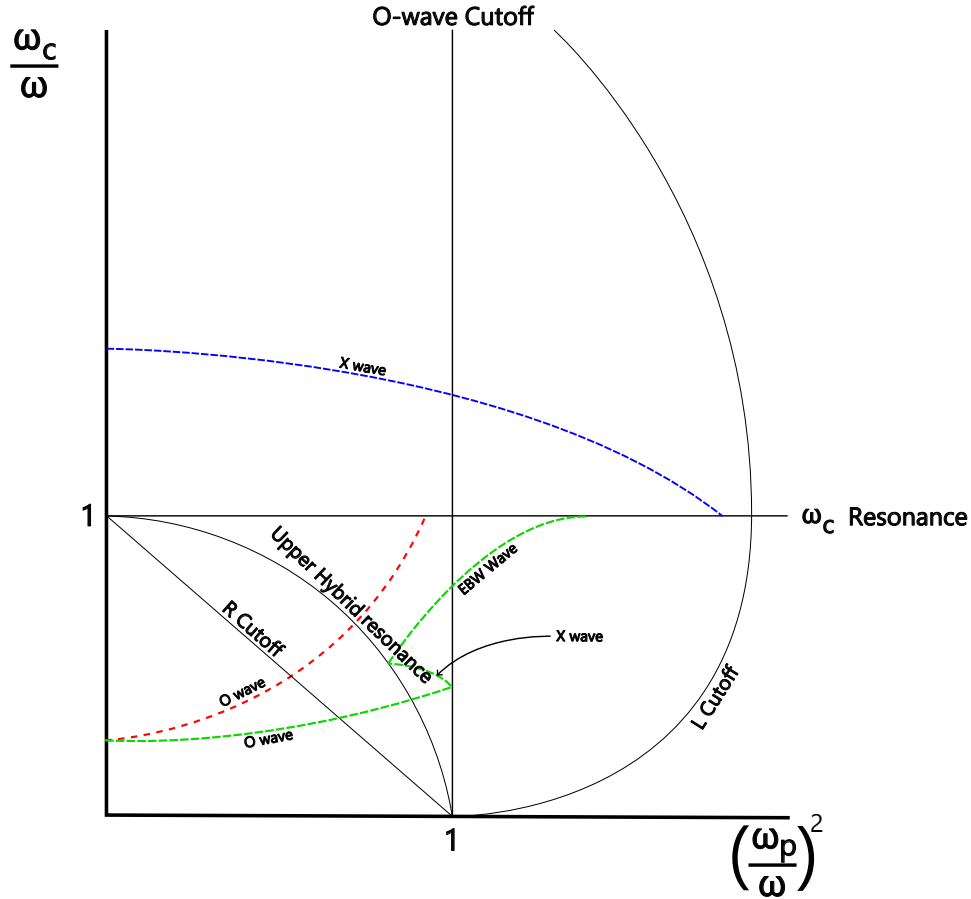
Figure 2.7: Part of a CMA diagram showing the cut-offs and resonances of the $O - wave$ and $X - wave$. The x-axis is proportional to the density of the plasma, while the y-axis is proportional to the magnetic field. The red dashed line shows how the $O - wave$ travels from the LFS to heat the plasma at the electron cyclotron resonance, while the blue dashed line shows heating by a $X - wave$ launched from the HFS. In the dashed green line, the OXB heating is shown for an overdense plasma; first, the $O - wave$ is launched from the LFS, at the $O - wave$ cut-off, the wave is converted to a $X - wave$ which travels until it hits the upper hybrid resonance, at which it is converted to an EBW, which can propagate through the plasma until it hits the electron cyclotron resonance, and therefore heats the plasma.

Chapter 3

Setup

The device NORTH is at DTU; see figure 3.1 for a picture. NORTH is a torus-shaped vacuum chamber with a major radius of $25cm$ and a minor radius of $12cm$. Figure 3.2 shows the axis of coordinates used in this paper. Eight toroidal field coils, with 12 turns each, are wrapped around the device at even spacing. There are four sockets in which a flange can be installed in the chamber. It is in such one the Langmuir probe is installed. The system is brought to a low pressure using a vacuum pump and a turbo pump when the pressure is low enough for that to work.
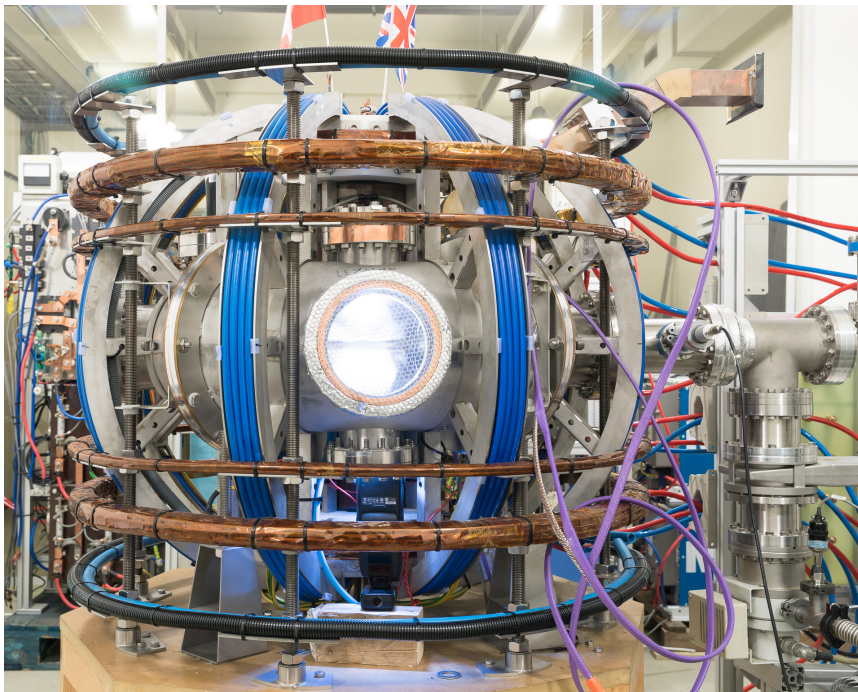
Figure 3.1: Picture of the device NORTH.
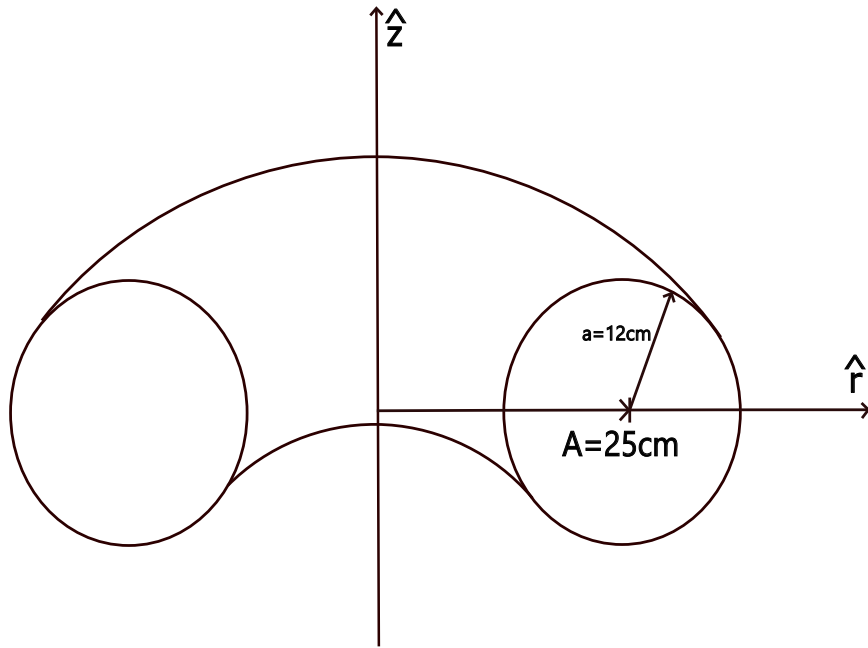
Figure 3.2: The position inside NORTH is referred to as the distance from the centre of the device.

The gas supply is easily changed between hydrogen, helium and argon by changing the connection tube to the chamber. When changing gas, the machine has to do a few runs before the data acquired is reliable, as there will be a bit of stray gas from the surrounding air when changing the supply gas, introducing impurities to the plasma. The plasma is powered using a microwave source at 2.45 GHz from either the low field side (LFS) or high field side (HFS). LFS is referring the magnetic field, which is low on the side furthest away from the centre of the device, and vice versa for HFS. If it isn't noted otherwise, we only power the plasma from the LFS in these experiments. The LFS microwave source is angled with respect to the magnetic field so that the chance for O-mode X-mode conversion is possible. The length of the shot (when the machine produces plasma), the pressure and the power of the microwave source can all be changed from shot to shot. We usually take shots of 1-second length at a pressure of $10^{-3}mbar$ with $900W$ of power.

A current is run through the toroidal field coils to generate the magnetic field inside NORTH. This current is $I_{Tf} \sim 1kA$. 4 Maxwell banks are used to power the toroidal field coils. Depending on the length of the shot, it can take up to multiple minutes to charge the Maxwell banks to full capacity again. As the Maxwell banks discharge during the shot, the current through the toroidal field coils is reduced. In figure 3.3, the toroidal field current can be seen.
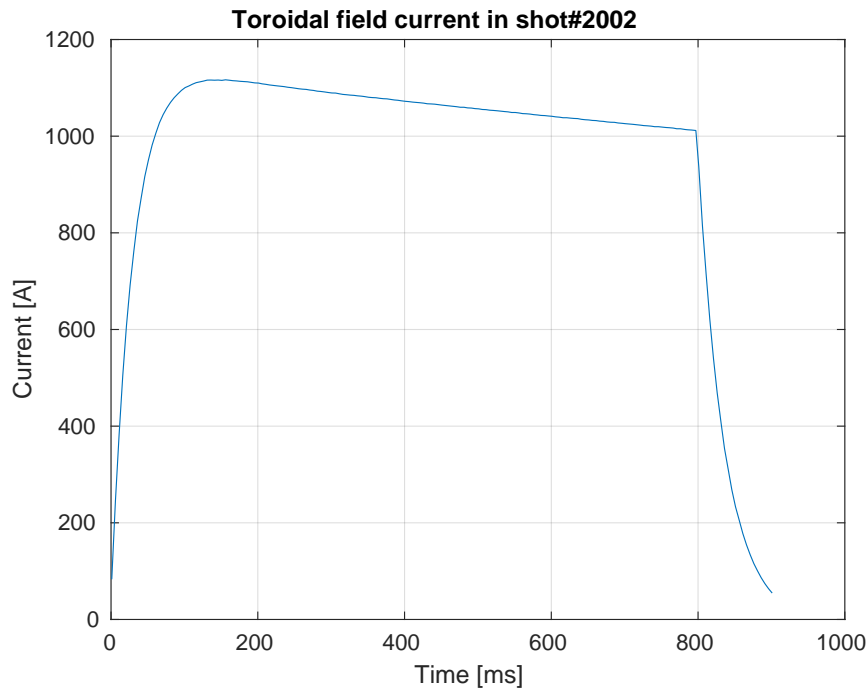
Figure 3.3: The toroidal field current is reduced during the shot, leading to a lower magnetic field strength in the device.

The control of NORTH is done using LabView[19] made by National Instruments.

Early setup

Before the Langmuir probe array was made, a single Langmuir probe was commissioned to get an understanding of the device. The single Langmuir probe was a cylindrical probe with a length of $2mm$ and radius of $\frac{1}{2}mm$. It was placed at the end of an electrical actuator, BLT45 Linear actuator, letting us control the probe's position.

Data acquisition

For data acquisition, we used a Red Pitaya Stemlab 125-10, 10bit. If we were measuring the ion saturation current, the Langmuir probe was biased using a TDK Lambda 300-11 power supply, with which we biased the probe at -50V. As the input of the Red pitaya can't be this large, the Red pitaya is floating at the same voltage as the probe. The Red pitaya can only take 16383 data points per shot at different preset frequencies, which meant that if we wanted to do a 1-second long shot, we could only measure at 15.6k

samples per second. When sweeping the voltage, we used a PXI 6040E card from National Instrument to generate a signal, which we ran through a 6826A Bipolar power supply from HP to amplify the signal $x10$ to end at the desired sweeping voltage. In experiments where we only swept at voltages close to 0 so that the measured signal has no absolute voltage over 10.5V, we can measure the data using another card from National Instruments; PXI 4472 DAQ 24bit. This card takes data at $102.4k$ samples per second for the whole experiment duration.

The signal from the Rogowski coil is measured using this NI card. All NI cards were placed inside a PXI 1000B chassis. The Rogowski coil is created at DTU, and the specific characteristics of the coil are unknown to me. The signal in the Rogowski coil is proportional to the change in current running through the coil.

Shortly before the new probe setup was made, a new single probe was made available. It was briefly used but found to have unstable signals.

Langmuir probe array

The new Langmuir probe array (Lpa) was designed and commissioned by me and constructed at DTU. The Lpa was made with a thin metal core with a diameter of $3mm$. Around this core was beads made of a ceramic material with an inner diameter of $3.4mm$ and an outer diameter of $5mm$. Between these beads and the core was insulated copper wires. These wires had a diameter of $0.15mm$. A tiny hole was cut in every second bead, from where a wire tip was taken out. At the end of the probe, a bolt was keeping all the beads in place tight. The bolt was coated so that it wasn't conducting. In total, 12 wire tips were taken out of the probe. A picture of the assembled probe is seen in fig 3.4. It was difficult to remove the insulation on the wires, of which we tried using acid and fire before grinding down a wire stripper so that the wires could be stripped down to the base of the probe. As the wires were fragile, some broke when we tried to strip them. For the same reason, not all wires are of the same length. A close picture of the probe tips can be seen in figure 3.5. The different wire lengths can be seen in table 3.1.

Amplifier circuitry

I built an amplifier circuit which we used between the Lpa and the data acquisition system. This circuit is seen in fig 3.6. This circuitry is similar to one used at TORPEX[1]. After the circuit had been tested on a breadboard, I made one of these circuits for each Langmuir probe in the Lpa and soldered them on a stripboard. The physical circuit is seen in fig 3.7.

In short, the circuitry removes the bias voltage from the input signal, amplifies it by a factor of 20.15 and filters out signals over $100kHz$.
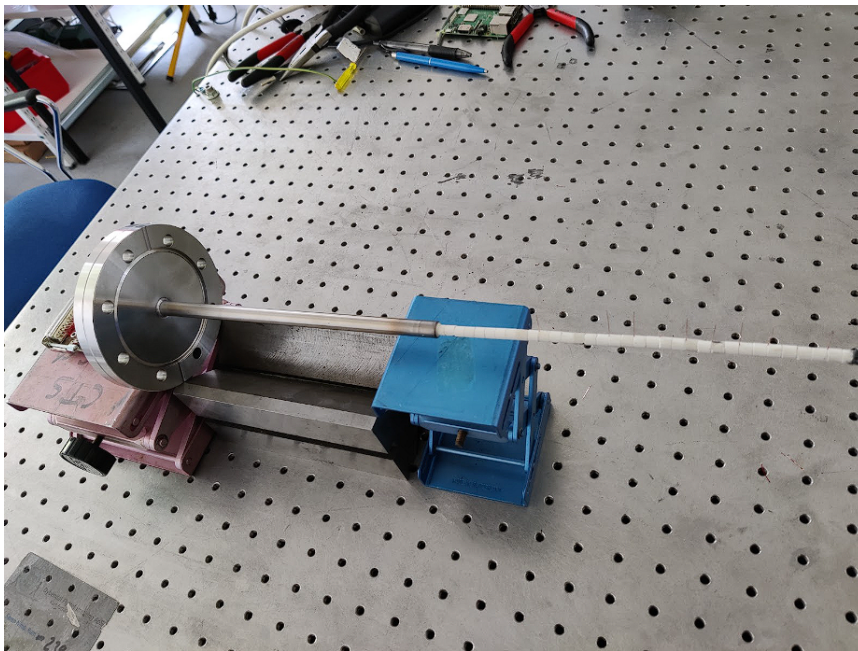
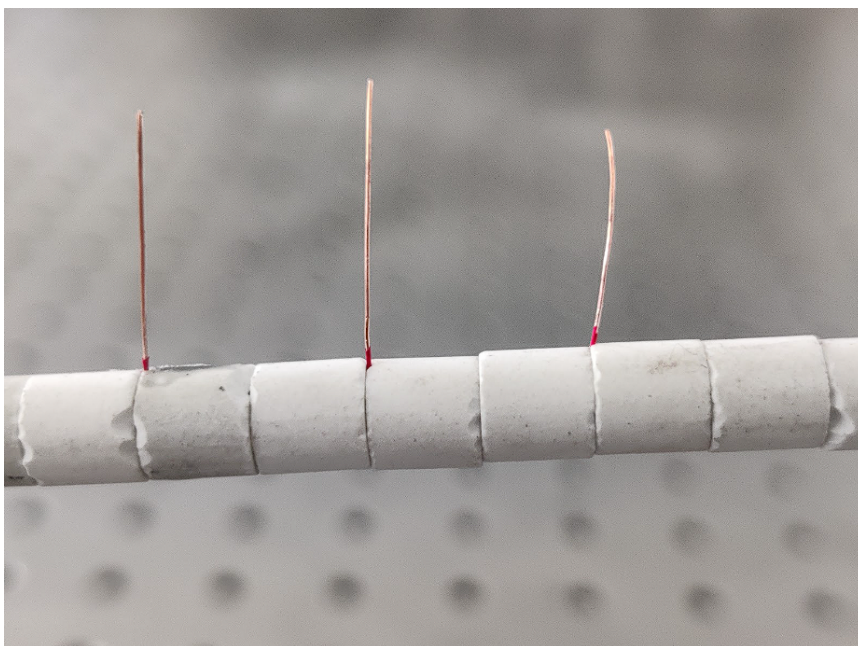Figure 3.4: The Langmuir probe array created and used in this experiment.

Figure 3.5: Picture of probe tips # 5, 6, 7 and 8, unfortunately, probe tip #8 is broken and therefore can't be seen on the picture.

Probe tip# (Length from probe end [cm])	Length [mm]
1	20
2	0
3	14.3
4	0
5	14.3
6	17.1
7	14.2
8	0
9	0
10	0
11	0
12	14.1

Table 3.1: The different wire lengths and their distance from the tip of the array.
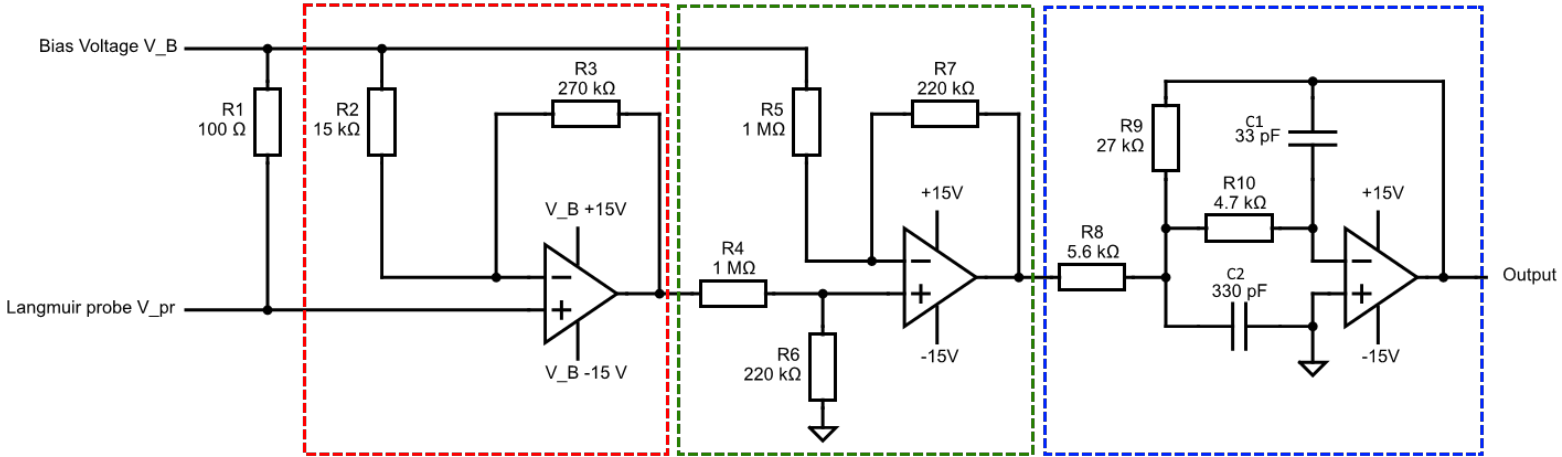
Figure 3.6: Diagram of the circuit used to isolate and amplify the signal.

Looking at fig 3.6, we provide the bias voltage and the probe voltage to the circuit and read a voltage as an output. To find the current running to the probe tip, we use Ohm's law while taking into account the 20-factor amplification:

$$I_{probe} = \frac{V_{out}/20}{R1} = \frac{v_{out}}{2000}$$

Referring to the coloured boxes in fig 3.6, the red box is a non-inverting amplifier which amplifies the voltage at the probe, V_{pr}, relative to the bias voltage V_B. The relative amplification is $A_{red} = 1 + \frac{R3}{R2} = 19$. In the green box, we have a differential amplifier, which in total removes the bias voltage
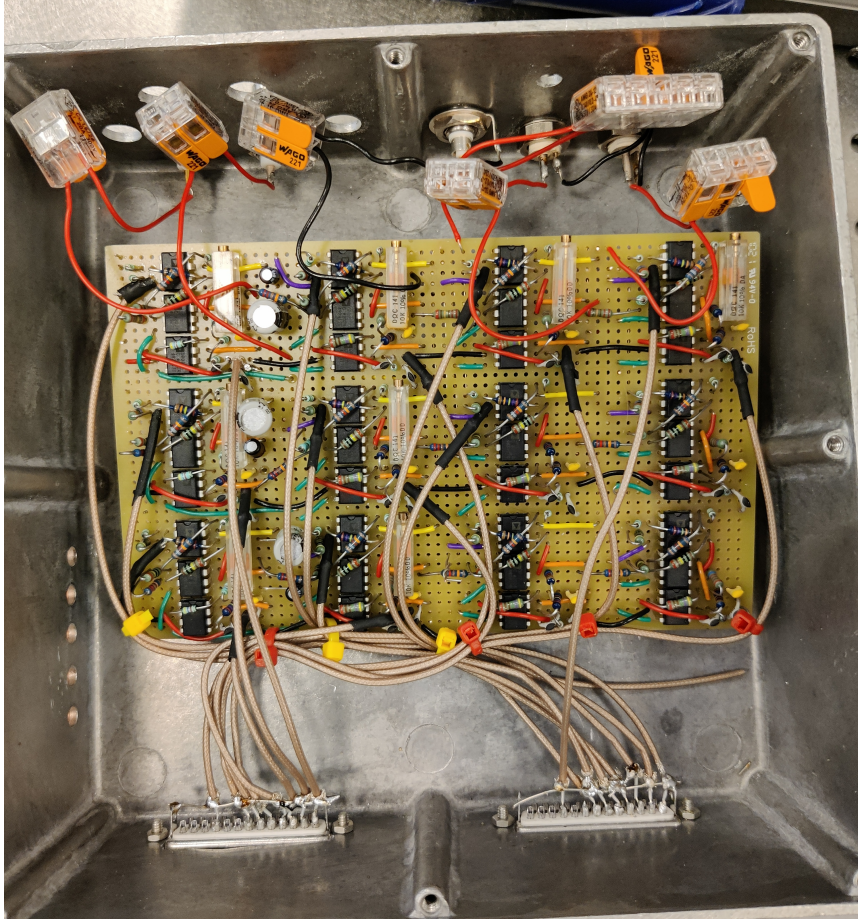
Figure 3.7: Picture of the circuitry board. This board can amplify 12 Langmuir probes.

from the signal while amplifying the signal with: $A_{green} = \frac{R7}{R5} = \frac{220k\Omega}{1M\Omega} \frac{1}{4.55}$. The blue box is a low-pass filter which amplifies the signal by $A_{blue} = -\frac{R9}{R8} = -\frac{27k\Omega}{5.6k\Omega} - 4.82$ at low frequencies, while it reduces the signal the higher the frequency of the signal[8]. In total, I have calculated the transfer function of the circuitry to be:

$$H(\omega) = \left(1 + \frac{R_3}{R_2}\right) \cdot \left(\frac{R_7}{R_5}\right) \cdot \left(-\frac{R_9}{-\beta\omega^2 + R_8 + i\omega\alpha}\right) \tag{3.1}$$

Using:

$$\alpha = C_1(R_8 R_9 + R_9 R_{10} + R_8 R_{10}), \tag{3.2}$$

$$\beta = C_1 C_2 R_8 R_9 R_{10}, \tag{3.3}$$

We find the gain as the amplitude of the transfer function as:

$$|H(\omega)| = \left(1 + \frac{R_3}{R_2}\right) \cdot \left(\frac{R_7}{R_5}\right) \cdot \frac{R_9}{\sqrt{R_8^2 - 2R_8\beta\omega^2 + \alpha^2\omega^2 + \beta^2\omega^4}} \quad (3.4)$$

At low frequencies, this reduces to:

$$A_{amplitude} = \left(1 + \frac{R_3}{R_2}\right) \cdot \left(\frac{R_7}{R_5}\right) \cdot \left(\frac{R_9}{R_8}\right) \quad (3.5)$$

Which with the component values as seen in fig 3.6, gives:

$$A_{amplitude} = \left(1 + \frac{270k\Omega}{15k\Omega}\right) \cdot \left(\frac{220k\Omega}{1M\Omega}\right) \cdot \left(\frac{27k\Omega}{5.6k\Omega}\right) = 20.15 \quad (3.6)$$

The phase shift can be found as the angle of the transfer function:

$$\phi = \angle H(\omega) = -arctan\left(\frac{Im(H(\omega))}{Re(H(\omega))}\right) = -arctan\left(\frac{-\alpha\omega}{R_8 - \beta\omega^2}\right) \quad (3.7)$$

This transfer function has a cutoff frequency of:

$$\omega_{cutoff} = \sqrt{\frac{R_8}{\beta} - \frac{\alpha^2}{2\beta^2} - \sqrt{2\frac{R_8^2}{\beta^2} - \frac{R_8\alpha^2}{\beta^3} + \frac{\alpha^4}{4\beta^4}}} \quad (3.8)$$

For the values seen on fig 3.6, this gives a cutoff frequency of:

$$\omega_{cutoff} = 125kHz \quad (3.9)$$

The cutoff frequency is the frequency at which the power transmitted is halved[8], and as the power scales with $P \propto V^2$, this is when the voltage gain is reduced by a factor of $\sqrt{\frac{1}{2}}$.

The frequency response can be seen plotted in fig 3.8.

The frequency response was also simulated using LTSpice, and found to be the same.

Frequency response from the actual circuit

A signal generator and an oscilloscope were used to measure the frequency response of the circuit build, by sending a set of sine waves with an amplitude of $100mV$ and specific frequencies into the amplifier, while the amplitude and phase shift of the output wave was measured. An example of a measurement is seen in fig 3.9. The average response of these amplifier circuits can be seen in table 3.2 and plotted on top of figure 3.8 in figure 3.10.

At the same time, the value of R_5 was fine-tuned. In place of the $1M\Omega$ resistor, a $680k\Omega-$, $270k\Omega-$, $47k\Omega$ resistor and a $5k\Omega$ potentiometer. This is important as the ratio of $\frac{R_7}{R_5}$ needs to be very close to the ratio $\frac{R_8}{R_4}$, as
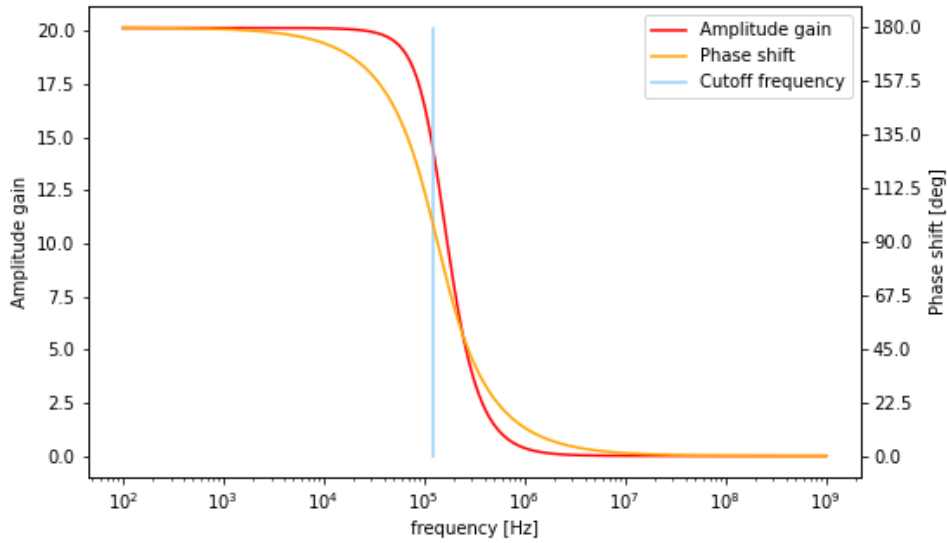
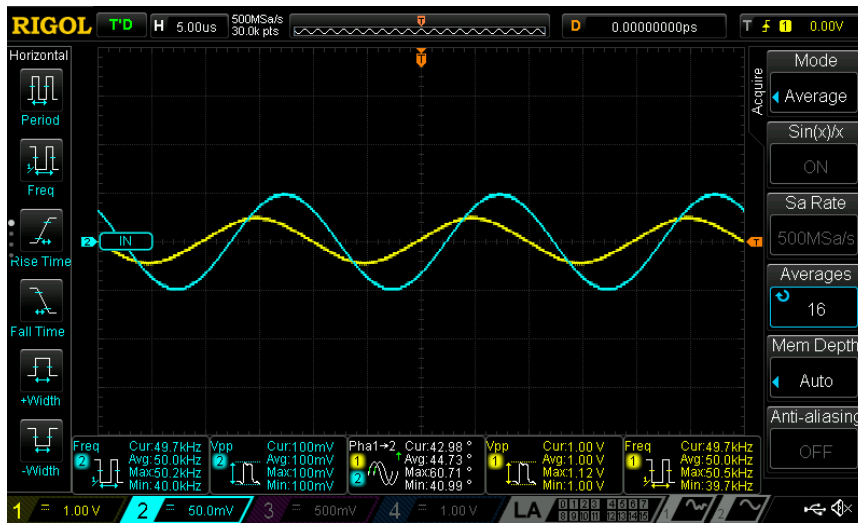Figure 3.8: Frequency response of the circuitry seen on fig 3.6.

Figure 3.9: Measurement of the frequency response of probe tip 1 of the Langmuir probe array.

otherwise, the difference between them will result in an offset in the signal proportional to the bias voltage. The potentiometer was tuned by testing the offset at 40V bias, comparing it to the signal at -40V bias, and then minimizing the difference. The signal was measured using an oscilloscope. All amplifier circuits were tuned so that the difference was less than $200\mu V$.

We can convert the measured voltage to the current flowing to the probe tips using the amplitude gain and the specific resistor values measured.

Frequency [kHz]	$\langle A \rangle$	A std	$\langle \Delta\phi \rangle$ [deg]	$\Delta\phi$ std [deg]
1	20.33	0.11	174	0.61
5	19.87	0.21	162	0.50
10	19.00	0.19	145	0.34
20	16.32	0.20	114	1.07
30	13.60	0.17	87.8	1.77
50	9.51	0.24	42.5	1.84
75	6.10	0.16	-2.20	2.97
100	4.38	0.12	-41.24	2.57
150	4.10	0.078	-184	5.54
200	0.810	0.090	-273	5.68

Table 3.2: Measured frequency response of the amplifier setup. A: Amplitude. $\Delta\phi$: Phase shift. Std: Standard deviation.
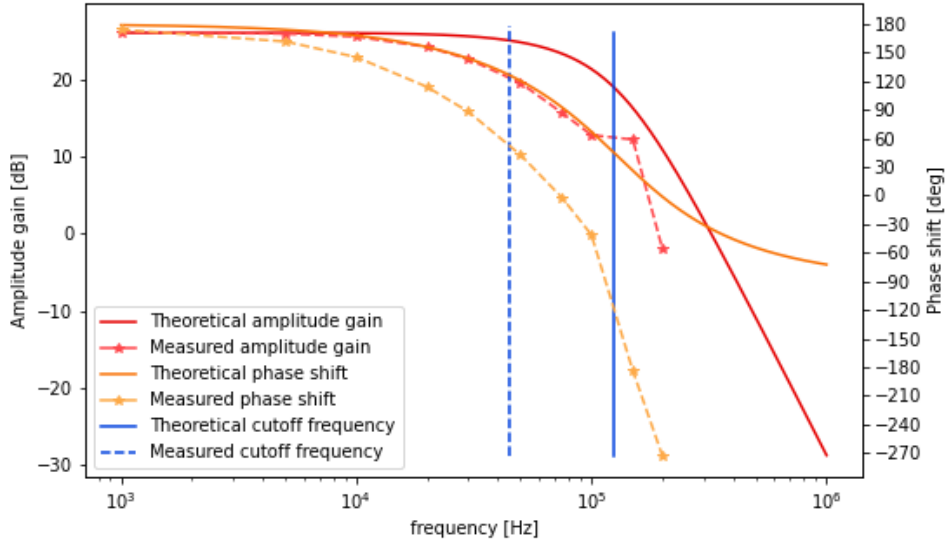
Figure 3.10: Calculated and measured frequency response of the amplifier setup.

Data acquisition

The data taken from the Lpa is recorded using a National instruments card. This card lets us save the data with $102.4kS/s$ for as long as we need, using up to 8 signals simultaneously. We can gain an increased sampling rate if we only use 2 or fewer signals. The card can take an input of up to $10.5V$, which in practice only means we can't measure the electron current, as the Ion saturation is much lower.

As we could only measure 8 signals at a time, we used 1 input for mea-

suring the applied bias voltage and 1 input to measure the signal from the Rogovski coil. The last 6 inputs were used to measure the signal from up to 6 probe tips from the Lpa.

Camera footage

During the project, it was briefly looked into whether a camera could be set up to record the plasma during the experiments through the glass at the front of NORTH. This was set up with a Raspberry pi 4 B and a Raspberry pi camera module. The goal was to record the plasma and see whether differences in the plasma density vertically and in time could be measured visually and held together with density measurements. The camera could measure at a maximum of 150 frames per second. However, the raspberry pi wasn't powerful enough to encode the video data at 150 frames per second, so the maximum frame rate captured was closer to 40. Due to significant differences in incoming light from the device and surroundings, the camera's contrast was hard to set at a functional level. When taking 150 frames per second, the resolution is 640x160. The resolution and the difficulties with the contrast settings lead me to put the camera closer to the device. This resulted in the camera breaking. Better results with a larger frame rate and a larger resolution are expected, using a better quality camera and a computer with more processing power than a Raspberry pi. Using a camera, we had hoped to be able to visually identify whether the plasma had denser areas than the rest.

Chapter 4

Results

Single Probe

The single probe has been used to gain an understanding of the device and the plasma created by it before the new Langmuir probe array is ready. Figure 4.1 shows a typical shot with the original probe.
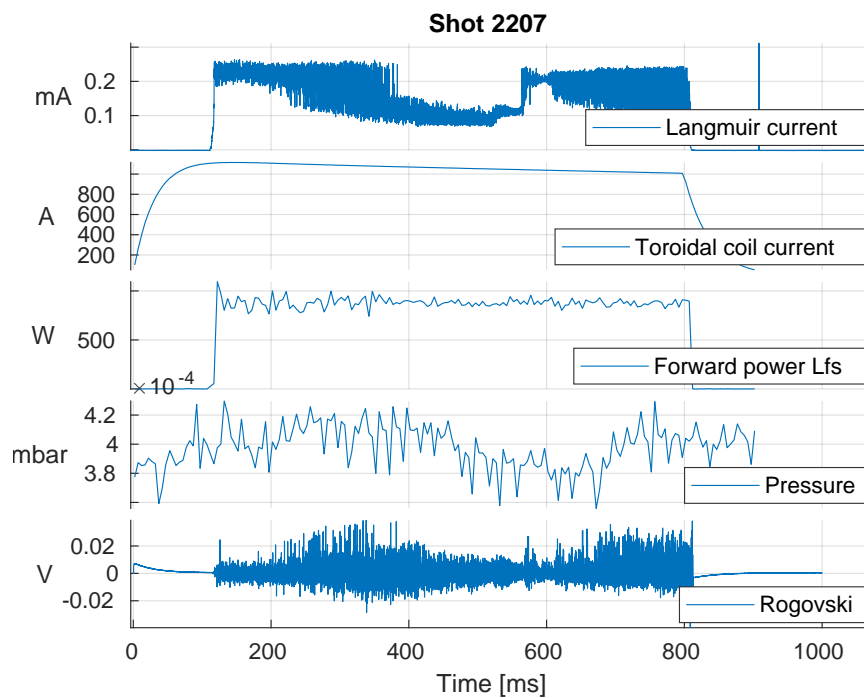
Figure 4.1: Shot number 2811 is seen. From top to bottom: Current measured at the probe, current through the tokamak coils, the voltage from the Rogowski coil, power inserted on the plasma through low field side microwaves and the pressure inside the device.

This shot is number 2207, where the probe is positioned in the centre of NORTH at $r = 25cm$. This shot measures ion saturation current by biasing the probe at $-50V$ during the shot. Under the assumption that the plasma temperature is constant, the ion saturation is proportional to the density of the plasma. In this shot, NORTH was filled with helium.

The Rogowski coil measures the magnetic field through it and is used as an extra way to confirm a shot is done correctly by confirming magnetic activity inside the device. If we had seen activity on the Langmuir probe without activity on the Rogowski coil, we would have to ensure the probe setup is not faulty.

From earlier experiments done at NORTH, the temperature is determined to be up to $20eV$ [14]. Assuming the temperature is constant throughout the experiment, the ion saturation current is proportional to the plasma density using equation 2.46. Figure 4.2 shows the density from shot #2208. As seen in the figure, the ion saturation is quite noisy. In this shot, the device uses hydrogen.
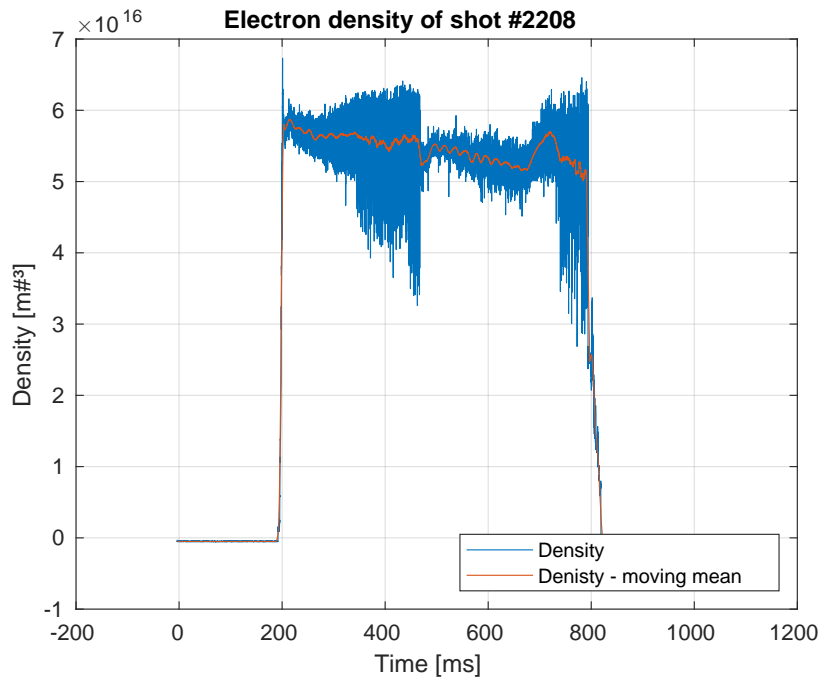
Figure 4.2: density of shot number 2208. The density is calculated assuming a constant temperature of $5eV$.

To determine the plasma's temperature, we sweep the voltage from -40V to 40V to make a current-voltage curve (I-V curve). Figure 4.3 shows a single sweep from experiment #2817. The temperature is found, by fitting 2.54 to the measured current, to be $4eV$. The sweep uses the National Instruments card to take the measurements, making it possible to take $102.4k$ samples

per second. The voltage is swept at $1000Hz$, which means there are 51 data points per I-V curve. As can be seen in the figure, the signal is only smooth at lower bias voltages. When the bias voltage gets larger than $\sim 5V$, the electron saturation dominates the signal, and we can't fit a proper function to the signal.
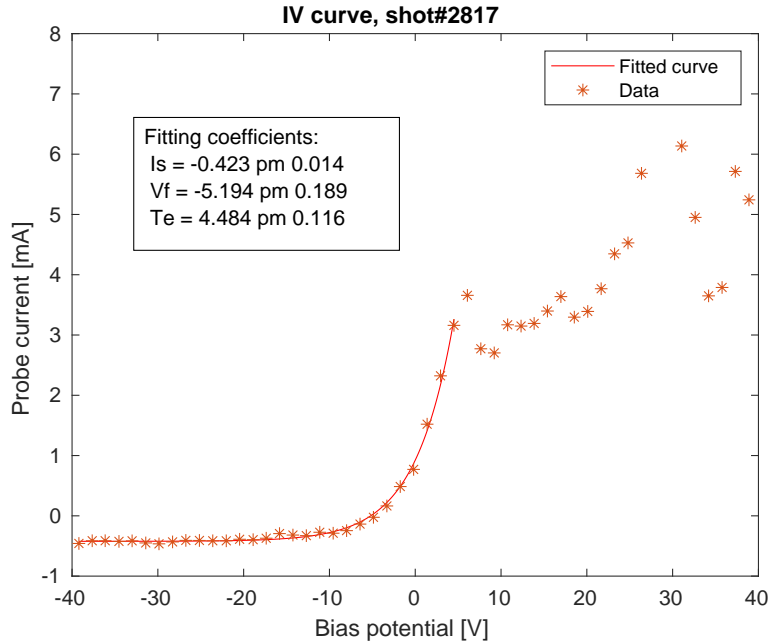
Figure 4.3: A single sweep from experiment #2817. The temperature, ion saturation and floating potential are found by fitting.

The complete shot is seen in figure 4.4. At the same time, the results of all the fitted sweeps during the experiment are seen in figure 4.5. Note that for $\sim 50ms$, a burst of high power was emitted from the HFS. The data in this section is ignored as the voltage received from the probe saturates at the maximum possible voltage the data acquisition can measure. The average density of the shot is $n = 2.09 \times 10^{16}m^{-3}$. The average temperature is $Te = 5.11eV$.

The power spectrum of the Rogowski coil is seen in figure 4.6. The most notable feature from the power spectrum is the lines at $20kHz$, $40kHz$ and just below $50kHz$. The $20kHz$ line is likely due to noise in the system, as the line is throughout the whole data set, even before and after the plasma is turned on. The $40kHz$ is just the next harmonic of the $20kHz$ line. The $50kHz$ line is more interesting, starting when the plasma is turned on. Then, when the power to the high field side is increased, it is reduced to $45kHz$.

We can profile the plasma characteristics using the single probe by moving the probe between experiments. In figure 4.7, the density profile is made
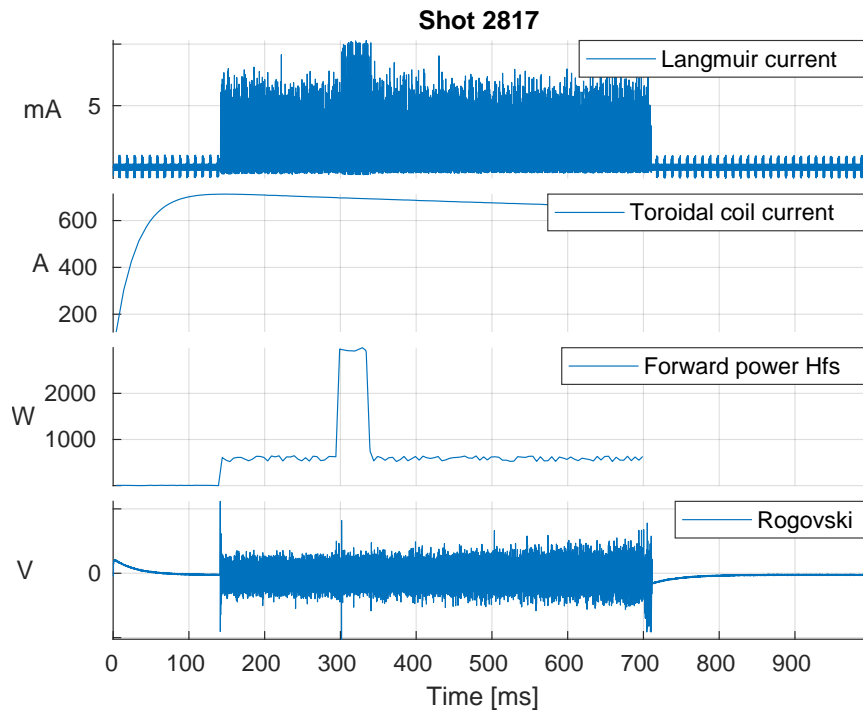
Figure 4.4: The data taken from experiment number 2817.
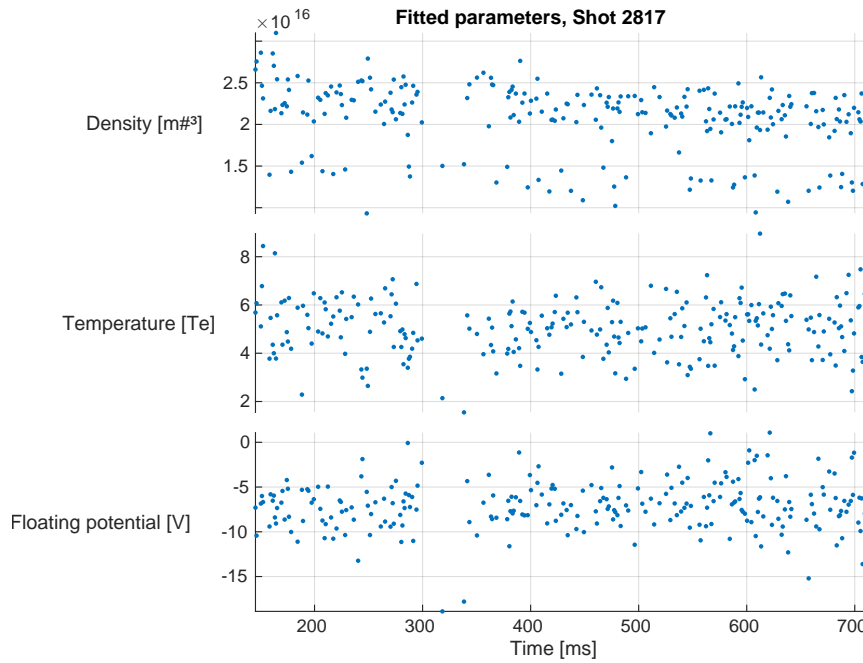
Figure 4.5: The fitted results from experiment number 2817.
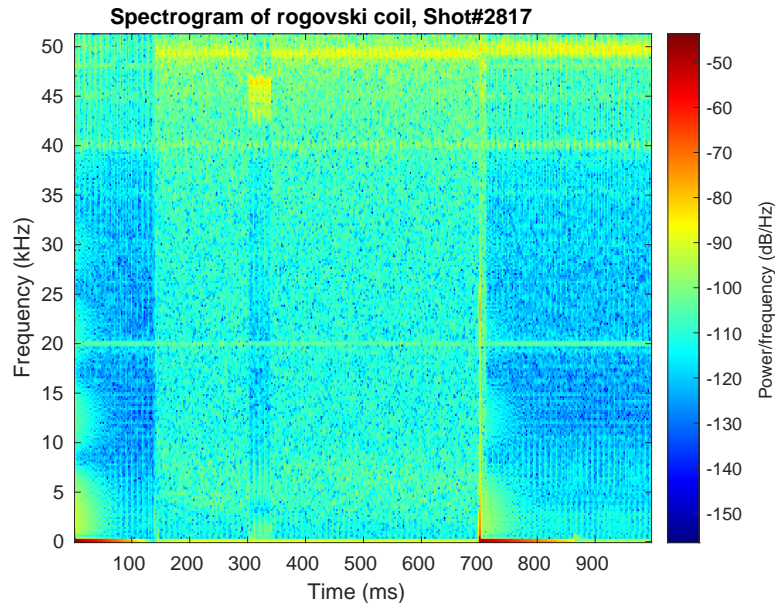
Figure 4.6: Power spectrum of the Rogowski coil from experiment number 2817.

from this method. The figure is made where the probe position, seen in the plots, is the distance to the centre of NORTH. This scan shows that the density of the plasma is highest the further inside the device you go and gets lower the further you go towards the outer wall. All the experiments are done with hydrogen, at $590W$, from the high field side. The sweeps are done at 1000Hz. All these experiments are done with the same settings for the device. Figure 4.8 shows the pressure during the experiments.

The floating potential can be seen in figure 4.9, while the temperature profile of the plasma can be seen in figure 4.10. As expected, the floating potential is negative since the electron moves faster than ions. The average electron temperature of the plasma is $Te = 4.83eV$. The temperature is close to uniform in the plasma, with a slight increase the further out of the device you go.
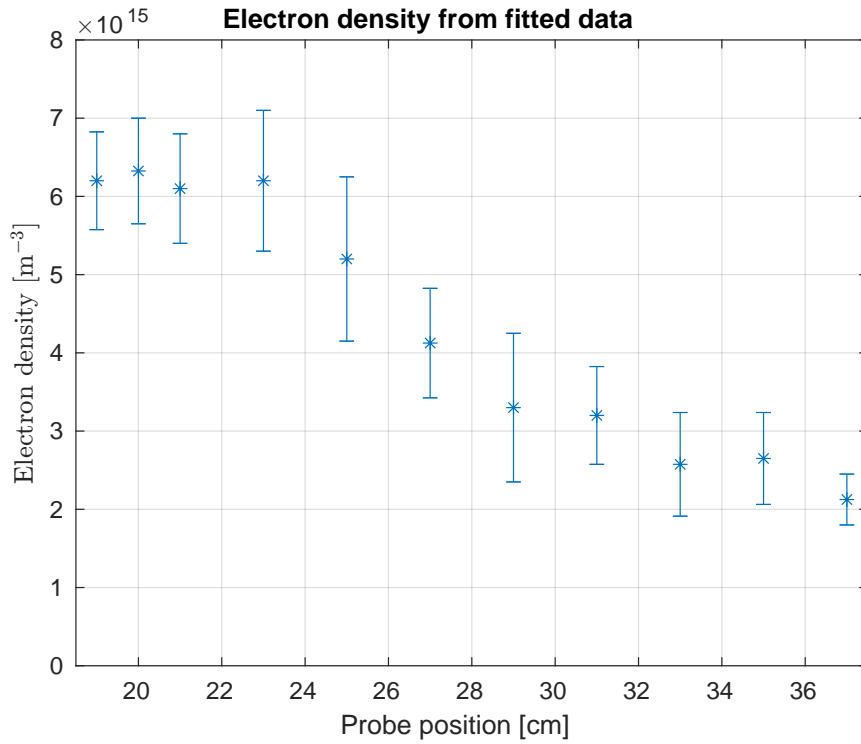
Figure 4.7: Density profile made from experiments with different probe positions.
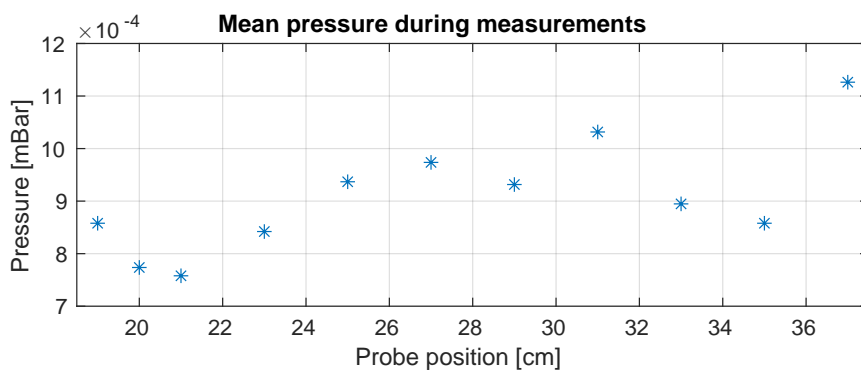
Figure 4.8: The mean of the pressure during the experiments at different probe positions.
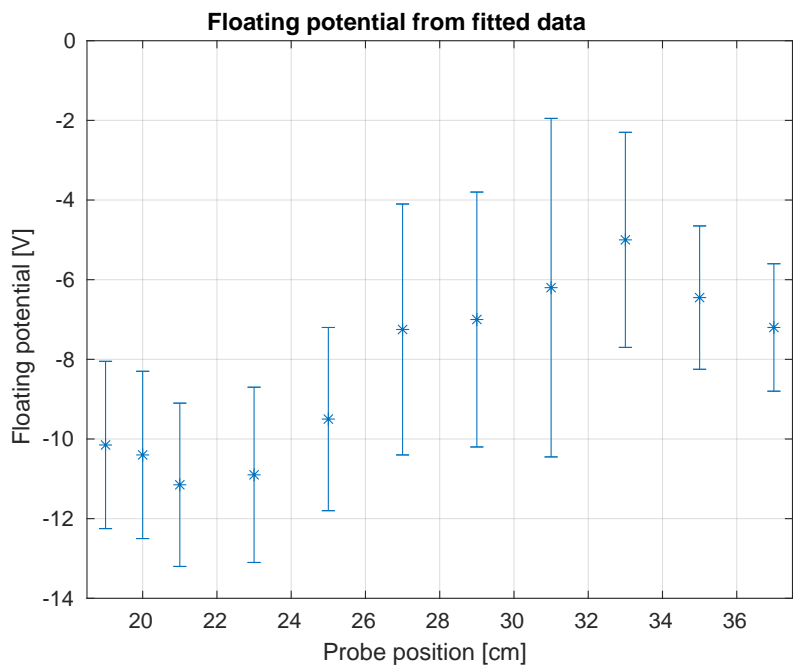
Figure 4.9: Floating potential profile made from experiments with different probe positions.
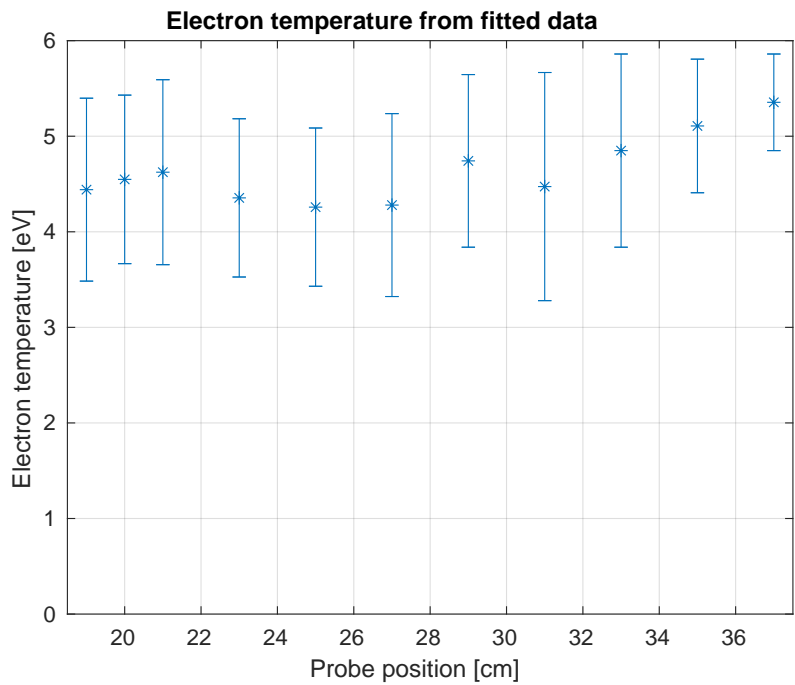
Figure 4.10: Temperature profile made from experiments with different probe positions.

Single probe - Modes

Using the single probe, we sometimes had experiments in which the signal had strong modes. With modes is meant that the signal oscillates at a specific frequency. An example is in figure 4.11, where the ion saturation current and the Rogovski coil have a mode at $7.4kHz$. This experiment is number 2201 and is done with hydrogen. The data is taken with the Red pitaya at $122k$ samples per second and therefore only for $0.135s$. The data acquisition starts just before the plasma is turned on. The following two harmonics of the $7.4kHz$ signal can also be seen. It is interesting that the mode can be seen in both the Rogowski coil and the ion saturation current, as this means that small perturbations in plasma current over time and the change in density are related.
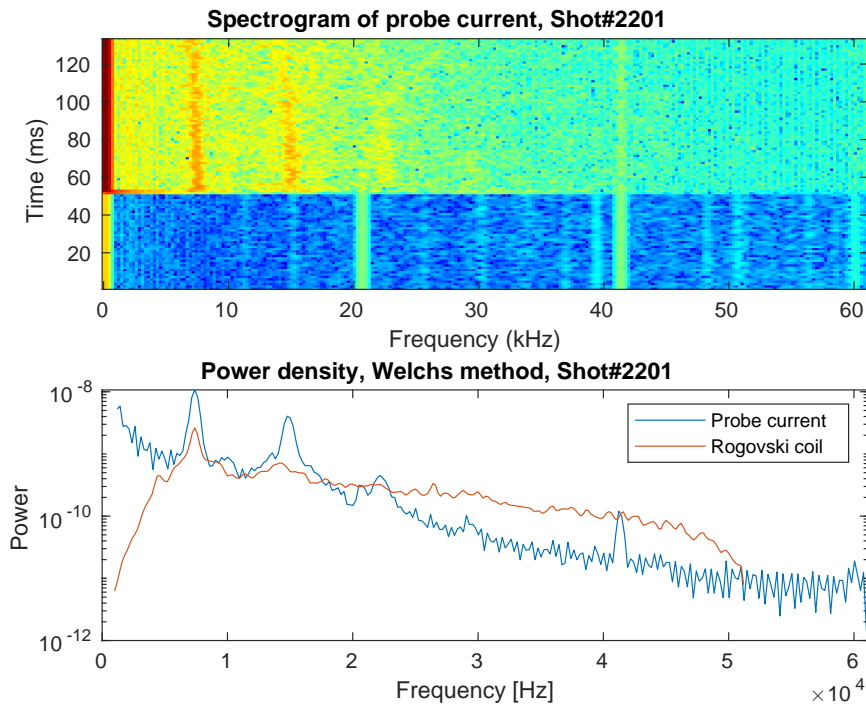
Figure 4.11: Top plot: Spectrogram of the ion saturation current, from which a mode at $7.4kHz$ and the corresponding harmonics of this frequency is easily identified. Bottom plot: Power spectrum of both the Rogovski coil and the ion saturation current. Both plots are made with data from shot #2201.

We do not know what contributes to the plasma having these modes. In figure 4.12, experiment number 2201 is repeated. On this spectrogram, we do not have a mode close to the $6.5kHz$ from the earlier experiment, but instead a faint signal at $50kHz$, in which the mode frequency reduces as

time passes. These two experiments have the same setup and settings and are done with only one experiment in between. The plasma density might be a reason, as the density of shot #2203 is $\sim 50\%$ larger than the density of shot #2201.
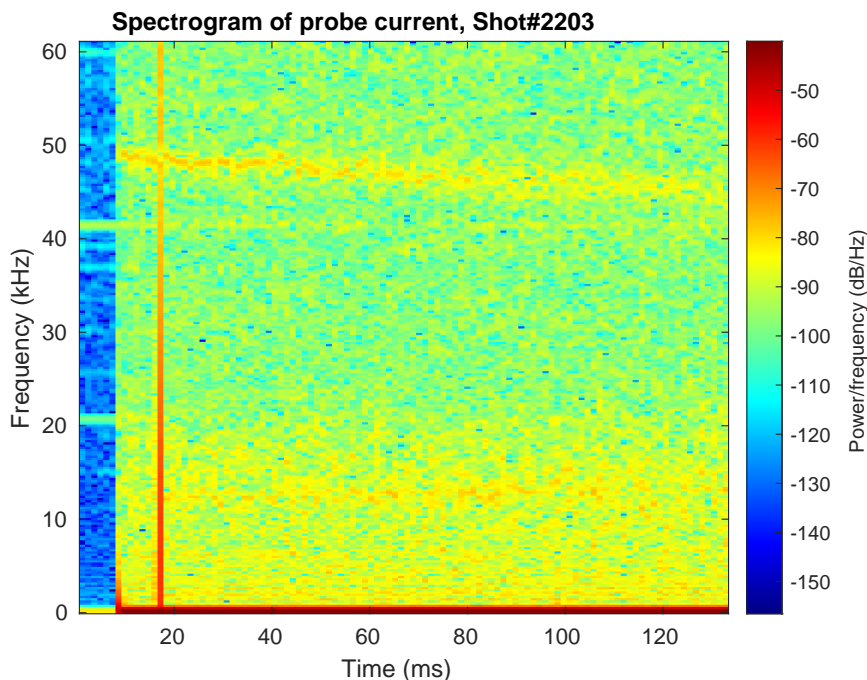

Figure 4.12: Spectrogram of the ion saturation in shot # 2203

This mode in the signal seems to be random and able to change within the experiment. The only way to influence whether there is a mode or not that we have found is to introduce a vertical magnetic field. In shot #2211, see figure 4.13, we have done the same experiment as number 2201 but have a current of $21A$ running through the horizontal coils to create a vertical magnetic field. This signal changes significantly over time, and as seen in figure 4.14, there are different changing modes in the ion saturation current and the Rogowski coil. We are taking data at $15.2k$ samples per second to record the whole experiment; this means we can't see modes at frequencies larger than $7.6kHz$. We see a $6.5kHz$ mode in the first half of the ion saturation current. This mode then increases in frequency until $t \sim 750ms$, where it drops to $\sim 2.3kHz$. In the Rogowski coil, we see the same modes as in the ion saturation current and the corresponding harmonics. The density of shot # 2211 is $\sim 15\%$ larger than that of shot #2201.
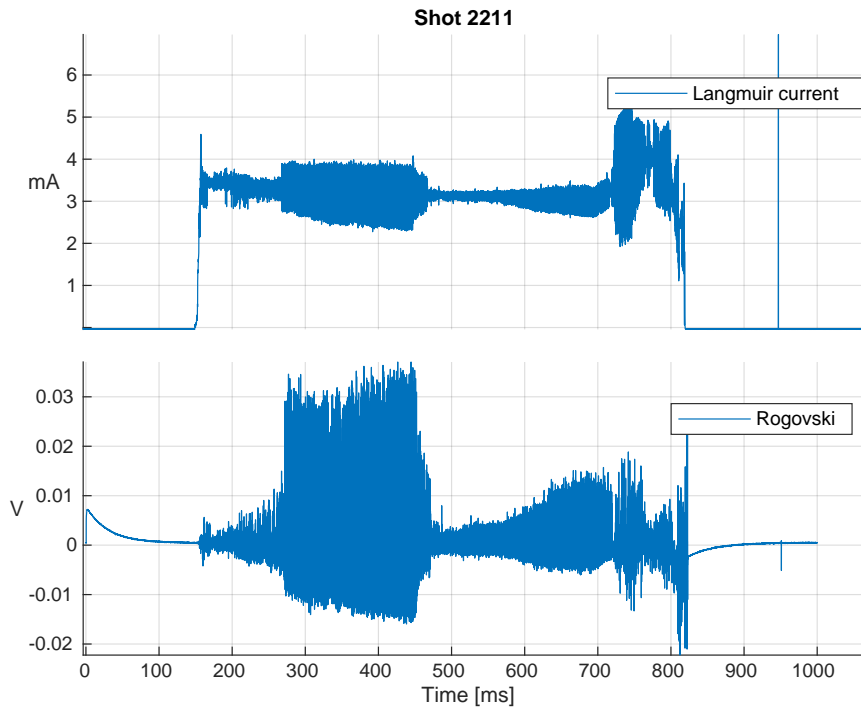
Figure 4.13: Experiment number 2211, the ion saturation current is seen to change over time.
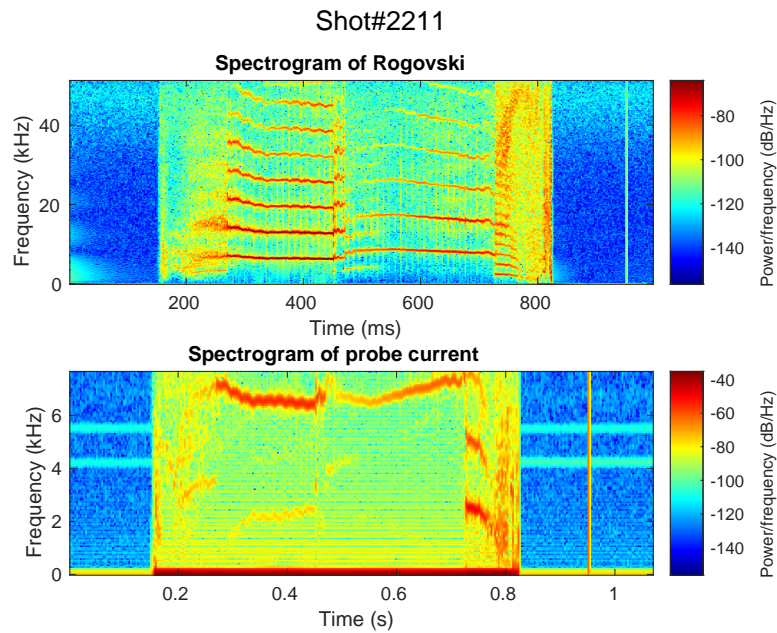

Figure 4.14: Spectrogram of experiment number 2211. There are strong modes during the shot.

New setup - 1D Langmuir probe array

We can now do the same experiments as we did for single-probe, but at multiple places simultaneously.

In figure 4.15, the plasma density is measured. The Langmuir probe array is swept at $200Hz$, from $-50V$ to $50V$. The gas in the chamber is helium. It can be noted from this figure that not only does the signal at the different probe tips change over time, but the relative density between the different probes also changes over time, meaning that the plasma changes not only the density over time but also its shape.
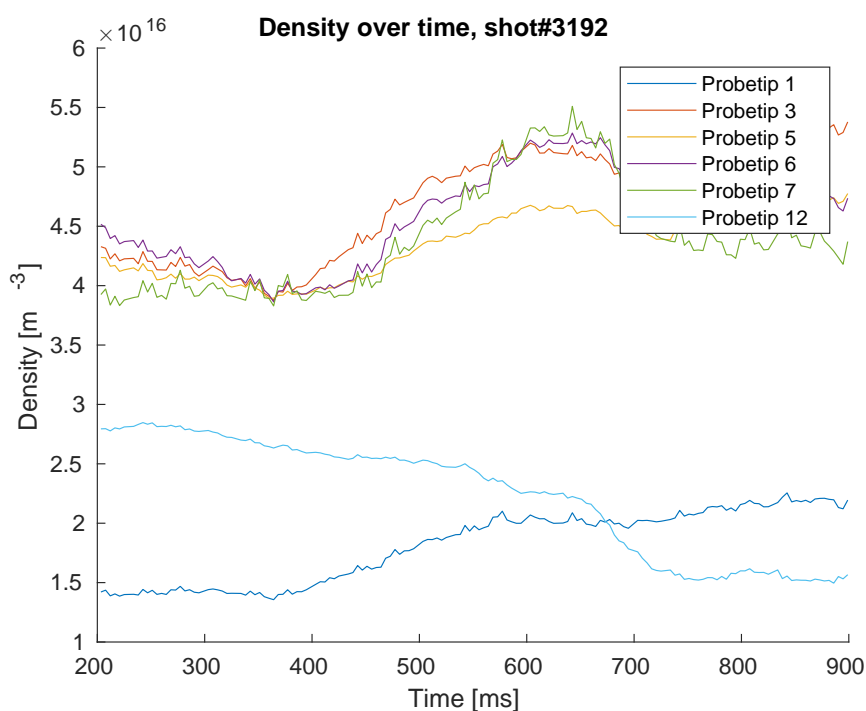
Figure 4.15: Density measured at different points simultaneously using the Langmuir probe array. The plot is a moving average.

Taking the average of this shot, a density profile has been made in figure 4.16. From this, it can be noted the main plasma body is confined at primarily $r = [25cm; 30cm]$.

Likewise, plots are made for the electron temperature in figure 4.17 and figure 4.18. From this, we see that the plasma has the largest temperature closer to the centre of the tokamak, and further out of the plasma, it drops in temperature over a few centimetres.
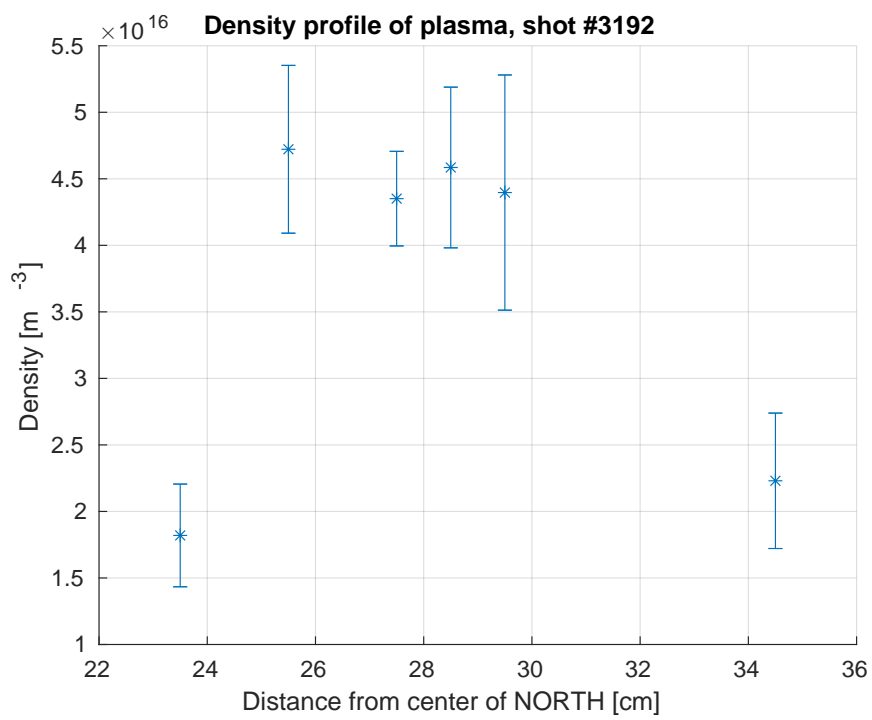
Figure 4.16: Density measurement found from IV curves. The error bars show the standard deviation of the density over time.
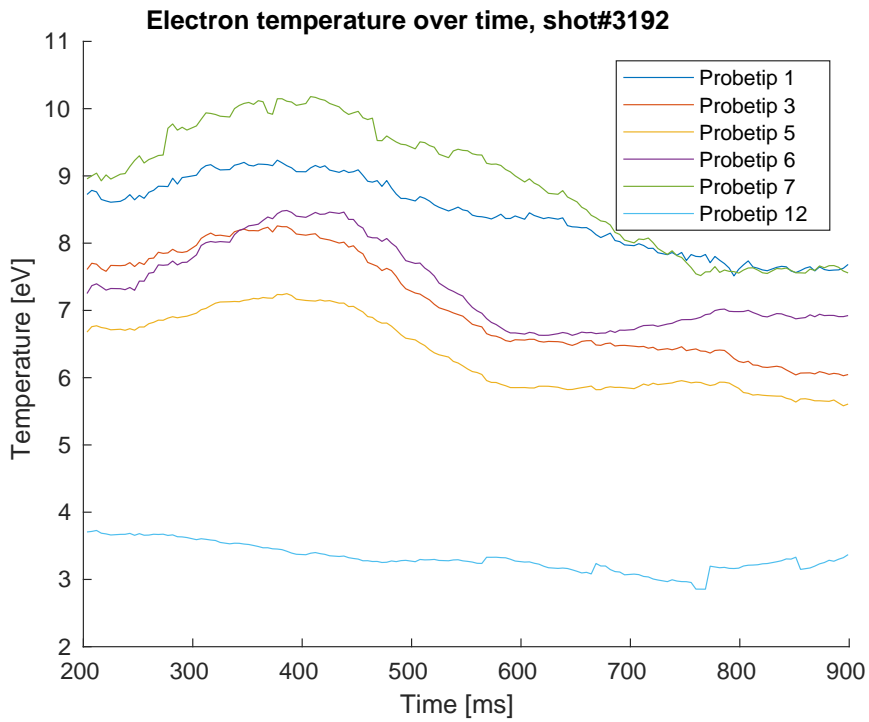
Figure 4.17: Electron temperature measured at different points simultaneously using the Langmuir probe array. The plot is a moving average.
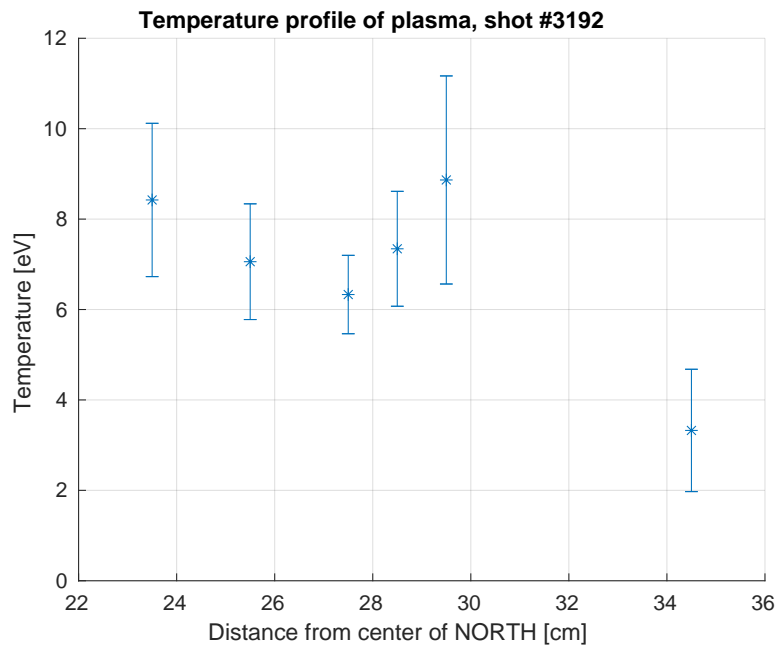

Figure 4.18: Electron temperature measurement found from IV curves. The error bars show the standard deviation of the temperature over time.

45

Blob transport

To detect blobs in the plasma, the Langmuir probe array is biased to $-50V$ so that the signal is proportional to the density of the plasma under the assumption of a constant temperature. In figure 4.19, this calculated density is de-trended by subtracting a moving mean with a window of 300 data points, normalized to the signal from probe tip 1, and plotted together with the signal from probe tip 2 and 3.
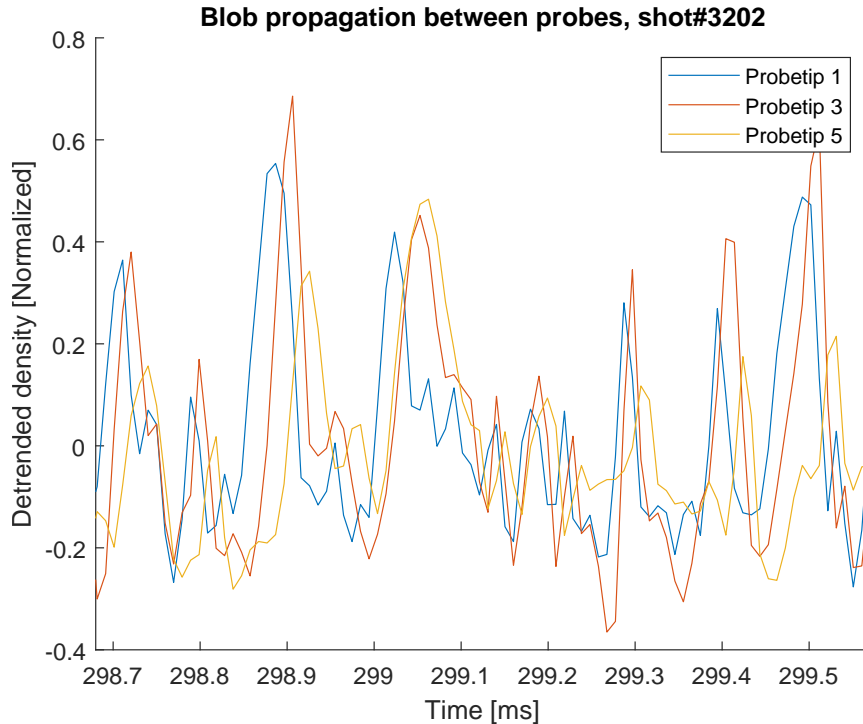

Figure 4.19: Subset of the de-trended normalized density measurement from probe tips 1, 2 and 3. Note that many of the peaks in each probe tip signals follow each other in the order of probe-tip 1, 3 and then 5.

In this figure, we can note that for every peak of a big enough size in the signal from probe tip 1, we have a peak from probe tip 3 shortly after and then a peak from probe tip 5 shortly after again. We can track the time when these peaks are measured to calculate the speed at which these blobs move. Unfortunately, each peak only spans a few data points since they are moving so fast, and we can only take data at $102.4k$ samples per second.

To classify blobs, I have done the following:

1. Each signal is normalized.

2. Each peak in the signal is found as all the points for which the neighbouring points are lower than the peak.

3. All peaks larger than a threshold value while spanning at least 4 points are kept, while the rest is discarded.

4. All these peaks are fitted with a gaussian distribution using the data from valley to valley.

5. The peaks from the different signals are compared. Peaks are considered part of a blob if a peak in probe tip 1 is followed by a peak in probe tip 3 before another peak is seen in probe tip 1. This peak in probe tip 3 then needs to be followed by a peak in probe tip 5 before another peak in probe tip 3. This continues at least until probe tip 6. The more probe tips we include, the more possible blobs are discarded.

6. Lastly, the speed of the possible blob is calculated from probe-tip to probe-tip by taking the physical distance between the probe tips and dividing it by the time between the peaks found by the gaussian fits. The blob is then accepted if the speed of the blob from probe tip 1 to 2 is not faster than five times the speed from probe tip 2 to probe tip 3 and not slower than $\frac{1}{5}$ of the same speed.

Since these blobs are measured at irregular times, these blobs are called irregular blobs in the rest of this paper.

In figure 4.20, a histogram of the radial velocities of these blobs from probe-tip to probe-tip can be seen. This experiment is number 3203, done with helium using a low field power of $900W$. From this plot, we see that in this shot, the blobs are slowed down the further out the blob travels.

Doing multiple of these for helium and hydrogen, we can create the velocity profiles seen in figure 4.21 and figure 4.22. It is seen from these plots that the blobs have the same behaviour of slowing down the further it travels in both helium and hydrogen, though it travels faster in hydrogen.

During these shots, probe 1 is positioned at $r = 23.5cm$. Probe 2 is $2cm$ further out at $r = 25.5cm$; probe tip 3 is $2cm$ further out at $r = 27.5cm$, probe tip 4 is $1cm$ further out at $r = 28.5cm$, and probe tip 5 is $1cm$ further out at $r = 29.5cm$. All the experiments are done at $900W$ power from the LFS.

The average velocity of the blobs in helium was $1940\frac{m}{s}$ while for blobs in hydrogen, it was $1260\frac{m}{s}$.

Figure 4.23 and figure 4.24 combine velocities from the first probe tip to the last and then plotted for a different amount of power from the low field side. It is interesting that for helium, the blobs travel faster the higher the power is, while for hydrogen, the blobs have the same velocity for $600W - 800W$ but travel slower at $900W$.
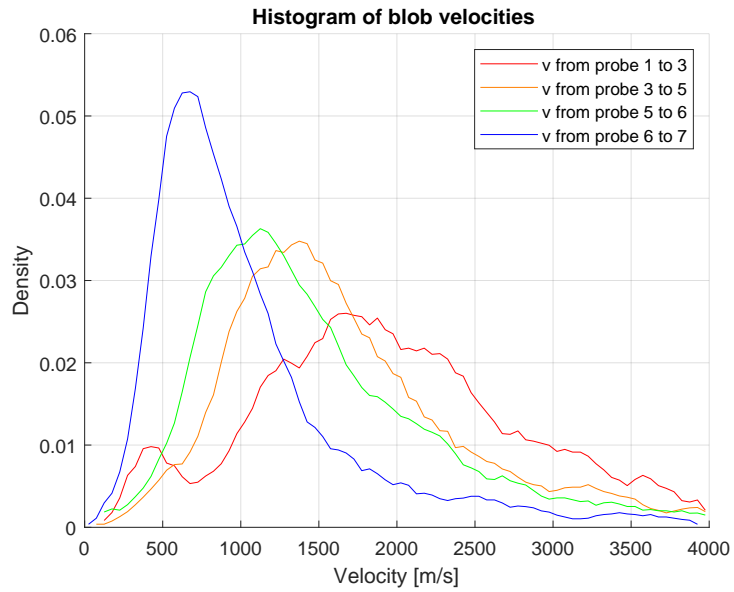
Figure 4.20: Histogram of radial velocities from probe tip to probe tip. Probe 1 is positioned at $r = 23.5cm$. Probe 2 is $2cm$ further out at $r = 25.5cm$; probe tip 3 is $2cm$ further out at $r = 27.5cm$, probe tip 4 is $1cm$ further out at $r = 28.5cm$, and probe tip 5 is $1cm$ further out at $r = 29.5cm$. This experiment is done with helium.

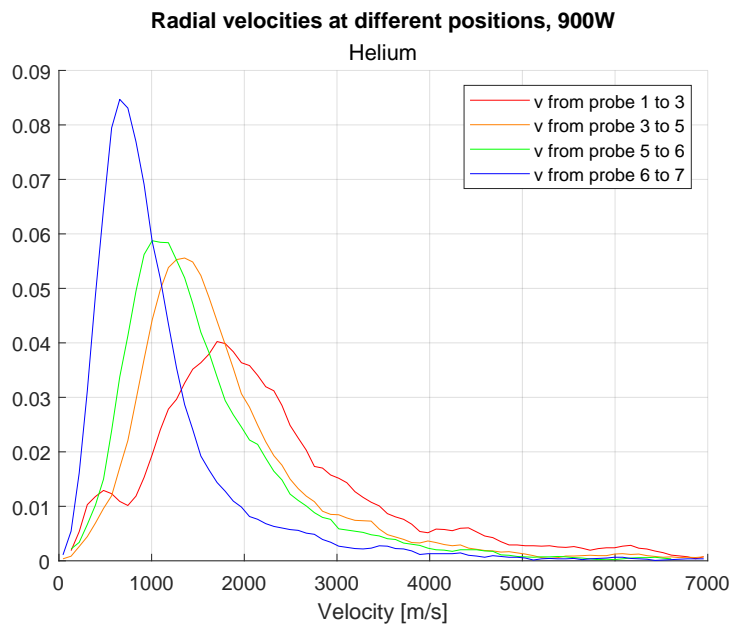Figure 4.21: Histogram of multiple experiments using helium at a low field power of 900W.
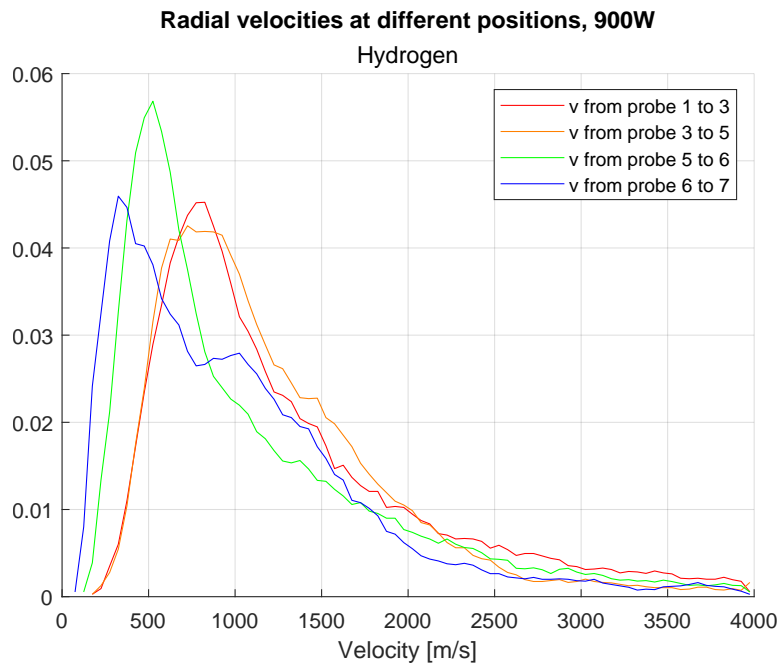
Figure 4.22: Histogram of multiple experiments using hydrogen at a low field power of 900W.
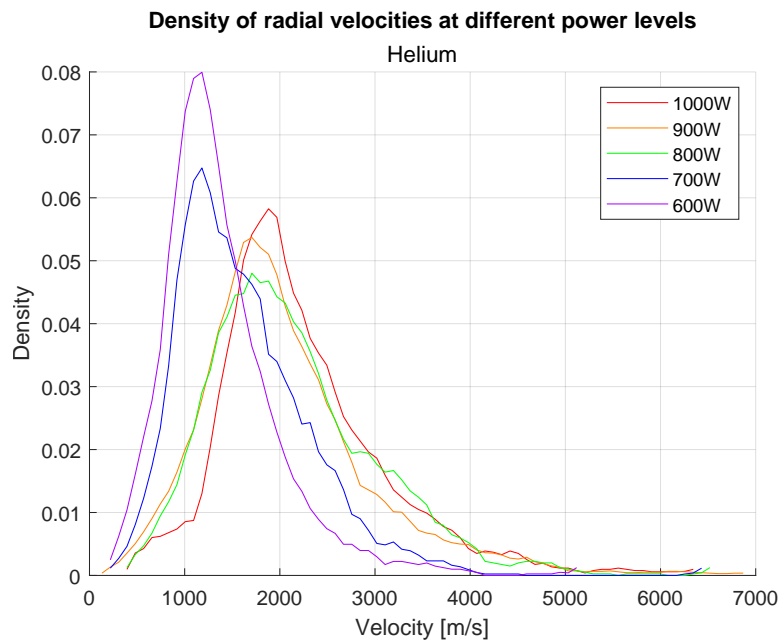

Figure 4.23: Histogram of multiple experiments using helium with a varying low field power
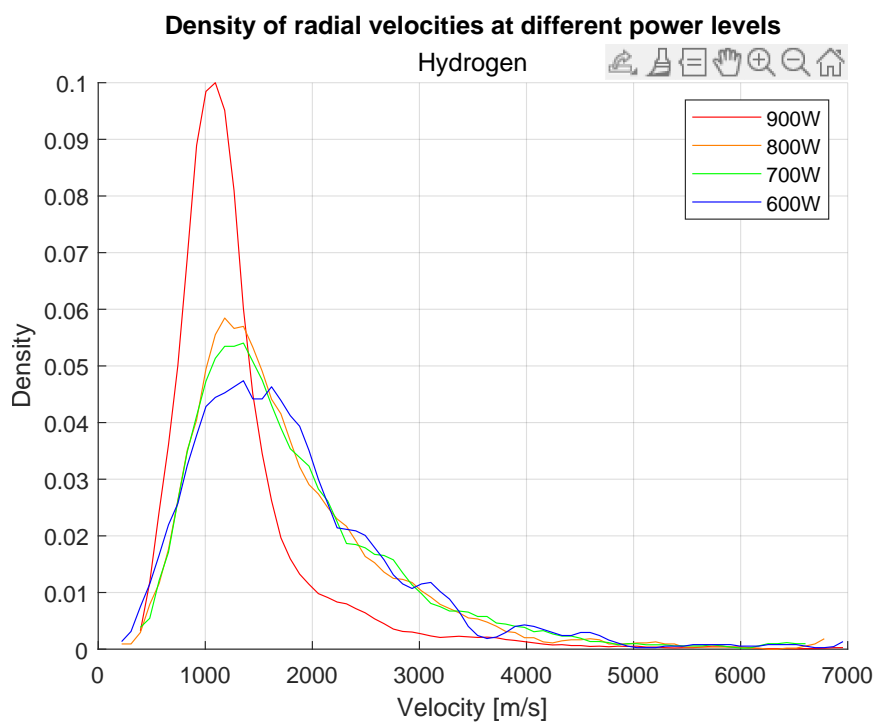
Figure 4.24: Histogram of multiple experiments using hydrogen with a varying low field power

Mode transport

Modes were also found using the multi-probe array. These modes are distinctive from other blobs in the plasma because they are measured at regular intervals. These blobs are also wider/move slower than other blobs, which means the probes have more data per blob from a mode.

In figure 4.25, a close-up of the irregular blobs and the periodic blobs from modes are seen. Due to the sampling rate, we can see more features of the periodic blobs, as they are wider and/or move slower than the irregular blobs.
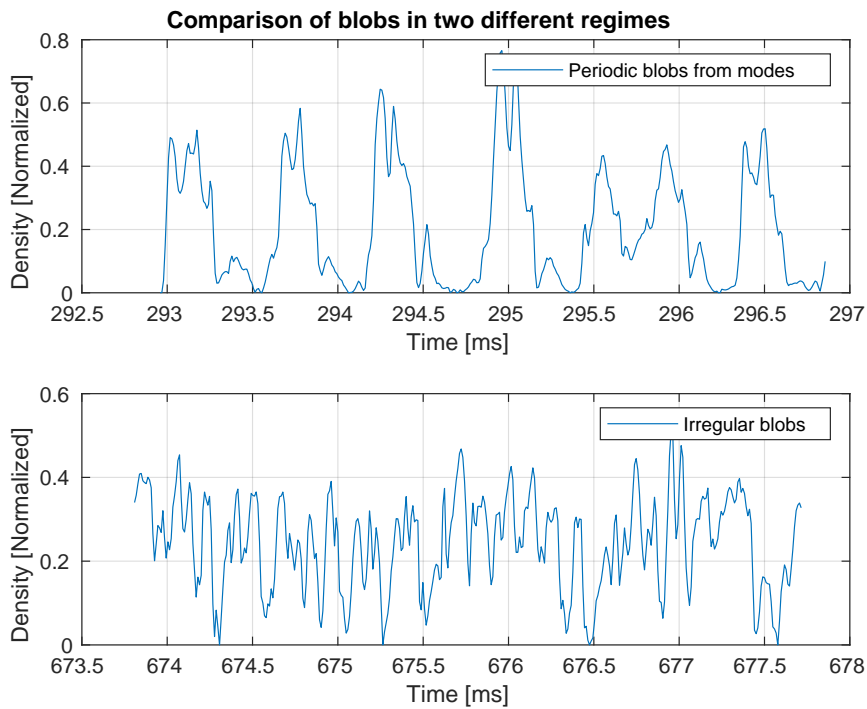

Figure 4.25: Close-up look at the density measured by probe tip #1 in shot 3222. The signal is de-trended and normalized. Top: Periodic blobs from modes during the beginning of the shot. Bottom: Irregular blobs from the end of the shot.

The velocity and size of these blobs were calculated as well. The velocity of blobs is found by measuring the phase shift between the signal from the different probe tips in a rolling window, which included ~ 5 blobs at a time, by fast Fourier transform. This phase velocity was then converted into the velocity at which the blobs travel. In figure 4.26, the velocity of these blobs is seen. The average blob velocity from modes in this shot is $v = 530 \frac{m}{s}$.

The blobs' width and height are also found during shot #3222. In this shot, there are both irregular and periodic blobs. The heights of the blobs
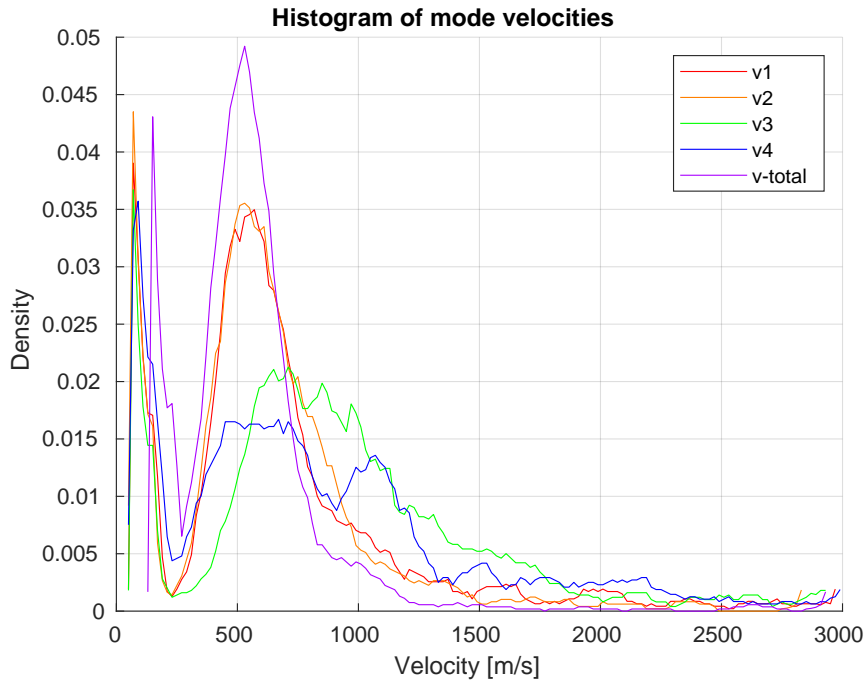
Figure 4.26: Histogram of the blob velocities from modes. $v1$ is the velocity from probe-tip 1 to 3. $v2$ is the velocity from probe-tip 3 to 5. $v3$ is the velocity from probe-tip 5 to 6. $v4$ is the velocity from probe-tip 6 to 7. While $v - total$ is the velocity from probe-tip 1 to 7.

are found by the prominence[1] of the blob's peak, while the width is found as the width at half prominence. In figure 4.27, the widths of the blobs can be seen for the whole shot; note that the plot in this figure is made as a moving mean of the calculated velocities. During the shot, there are clear modes in the signals from $t = 300ms$ to $t = 400ms$, then there is an area where there sporadic are periodic blobs while there otherwise are irregular blobs, while at the end, after $t = 700ms$ are purely irregular blobs.

It is interesting to see that the width of the periodic blobs is getting thinner the further out in NORTH they travel, while (if we ignore the measurement from the first probe tip) it is reversed for when there are only irregular blobs.

The height of the blobs be seen in figure 4.28

It can be noted that the heights don't change much relative to each other. The exception is heights measured at probe-tip 7, which decreases throughout the whole shot and doesn't follow the trend the other probe-tips see, where the height changes at different rates.

---

[1]The prominence is the height of the peak relative to the surrounding signal.
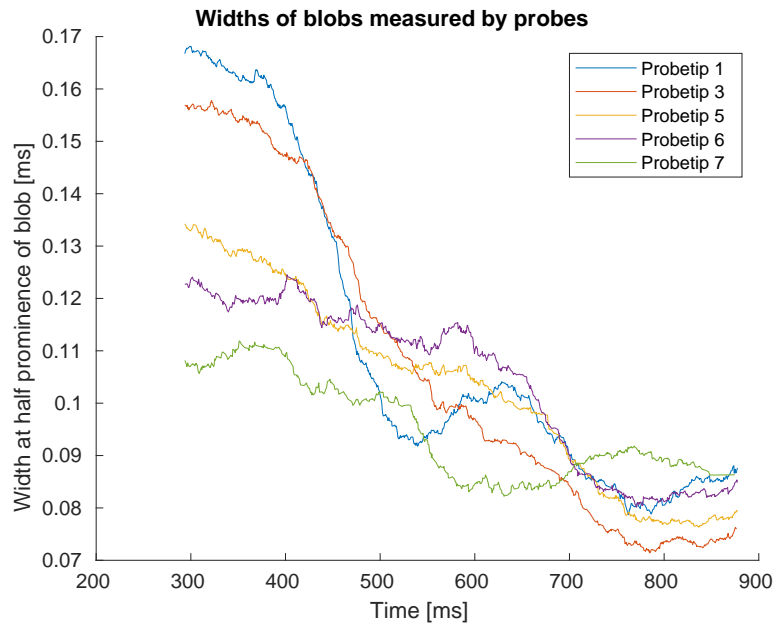
Figure 4.27: The widths of the blob during shot #3222. The widths are calculated as the width of the blob at half prominence.
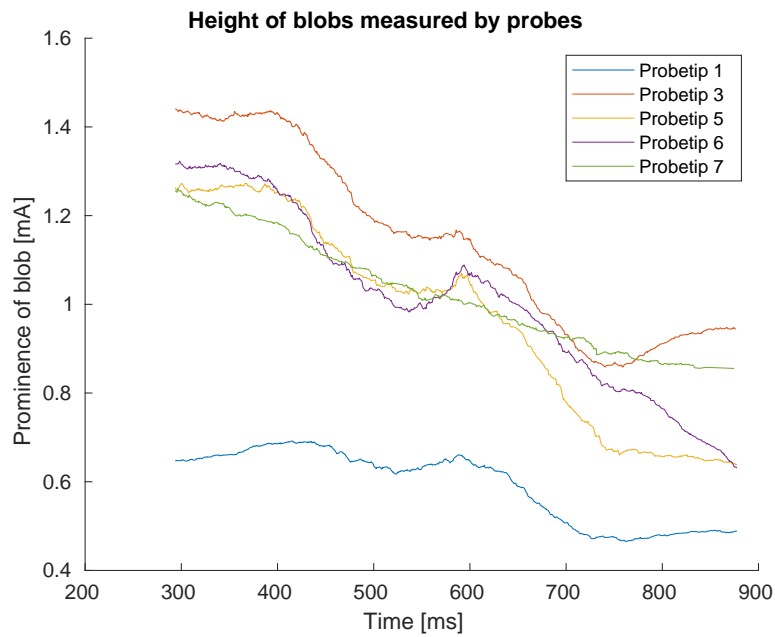

Figure 4.28: The heights of the blobs during shot #3222. The heights are calculated as the prominence of the blob.

Chapter 5

Discussion

Density and temperature profiles

When comparing the plasma density profile using the single probe, see figure 4.7, and the Langmuir probe array, see fig 4.16, they are both of similar shape and size. This indicates that the Lpa is working as intended, even though some probe tips are missing while others are different sizes than the rest. Even though the amplifier setup was shown to work outside of plasma and in simulations, it is usable even though the circuit's frequency response was measured to be lower than what it should have been, as seen in figure 3.10. The reason the frequency response was lower than expected could be due to the use of components with a too-high tolerance. However, it is much more likely that the most significant reason it doesn't perform as expected is the operational amplifiers used in the setup. The operational amplifiers used have a gain bandwidth product of $600kHz$. This means the cut-off frequency is lowered because the amplifier cannot "keep up". In the setup's first amplifier, the gain is 19, which gives a cut-off frequency of $\frac{600kHz}{19} = 31.5kHz$. The cut-off frequency is further lowered as multiple operational amplifiers are in series. Creating new circuitry using operational amplifiers with a higher gain bandwidth product would be interesting and likely give a better frequency response.

The density profile acquired from using the single probe, as seen in figure 4.7, is similar to earlier results made by student Nicklas Erichsen Kihm on the same machine (see appendix A). At the same time, the density profile using the single probe from figure 4.7 and the new Lpa from figure 4.16 are similar as they are in the same order of magnitude while having a similar profile shape. The two shown profiles have different gas used, so they can't be expected to have the same density. Both profiles have a low density on the low field side and increase until the centre of the plasma. The Lpa then have a significant drop-off at the probe tip closest to the high field side of

the device. This could be due to the plasma having a different point for resonance heating leading to a different density profile. The same is true in the case of temperature. The differences in probe tip length could also be problematic as if our assumption that edge effects from the probe are minimal isn't valid; the differences in probe length then lead to differences in edge effects, which could increase the collection area of some of the probe tips more than others. It would be possible to test the effect of different probe-tip lengths if the Lpa was put on an actuator so that the position in the plasma could be changed. Then by comparing the profile measured at different positions, the signal from each probe tip could be calibrated.

Another thing is that as the probe is larger than the earlier probe, it should be tested to determine whether the probe array is large enough to perturb the plasma, reducing the usefulness of the data taken. This could be done by simultaneously having both the Lpa and another probe inside the plasma and doing different shots where the probes have different positions. If the plasma parameters don't change whether the probe is inserted into the plasma, it would mean that the Lpa doesn't perturb the plasma. Based on previous results, it is assumed that it doesn't perturb the plasma as it isn't much bigger than the old probe and finds the same results. It should also be possible to do simulations to determine how much the Lpa will perturb the plasma.

As touched briefly upon, the camera used to try to get video data from the plasma wasn't feasible. The Raspberry Pi used as the computer was too slow to capture the data at a high frame rate, while the video captured by the camera was low resolution. The camera's contrast wasn't easy to set right, meaning it had to be closer to the chamber, which resulted in it breaking. It would be interesting if a proper setup were made to monitor the plasma during shots. Better hardware would solve the problem of low resolution and frame rate, while some solution for the contrast of the video must be found. A possible solution might be to encase the camera and put it on one of the flanges to shield it from outside light.

Transport at NORTH

Using the Lpa, two different types of blobs were identified. "Irregular blobs" were measured in the plasma at seemingly random times, and "periodic blobs" were detected at a close to constant frequency. See figure 4.25 for a close-up of both types of blobs. The periodic blobs span more data points than the irregular blobs though this doesn't mean they are of different widths, as the blobs travel at different velocities. The Irregular blobs have an average velocity of $1940\frac{m}{s}$ in helium and $1260\frac{m}{s}$ in hydrogen. While

the periodic blobs have an average velocity of $530\frac{m}{s}$

According to an article by R. Kube and O. E. Garcia[10], the velocity of blobs are up to one-tenth of the sound speed. Under the assumption of cold ions, the sound speed is calculated as follows:

$$v_s = \frac{\gamma_e Z T_{eV}}{M}$$

Where $\gamma_e \sim 1$, Z is the atomic charge number, M is the mass of the ion forming the plasma, while T_{eV} is the plasma temperature. Taking the temperature to be $8eV$ as per the temperatures from figure 4.17, we find an acoustic velocity of:

$$v_s^H = 28\frac{km}{s}$$

for hydrogen, and:

$$v_s^{He} = 20\frac{km}{s}$$

for Helium.

This means that the average blob velocities we found are 9.7% of the sound speed for helium and 4.5% for hydrogen for irregular blobs. The average blob velocity of periodic blobs is then 2.7% of the sound speed. All were within one-tenth of the sound speed, as reported by R. Kube and O. E. Garcia. It is high for helium as it was 9.7% for the average, meaning some blobs were likely propagating with an even higher velocity. This might be due to uncertainties in calculating the velocity, as there were only a few data points for each blob per probe. Better diagnostics must be made to verify if the blobs propagate at this speed. A high-motion camera might be able to detect blobs if placed correctly, as it is done in the article.

The profile of the blobs was determined by averaging the different blobs. This can be seen in figure 5.1 for irregular blobs. This was made by taking the times for the peaks of the blobs, which were determined when the blob velocities were calculated, and then taking the nine closest data points and, after removing offsets and normalising the size, averaging all the blobs together.

As can be seen in the figure, the profile looks very gaussian, though with different starting and ending levels.

The profile looks quite different when the same is done for periodic blobs. In figure 5.2, the profile for periodic blobs is shown. This profile has a sharp rise, and a slower descent, compared to the irregular blobs. These blobs also have multiple peaks as well.

It was hoped that the profile of the blob would look like the profile O. E. GARCIA has shown in his paper "Blob Transport in the Plasma Edge: a Review"[7] of data from TCV[6] and ESEL[15]. The blob profile from his article can be seen in appendix B. It is seen that the periodic blobs
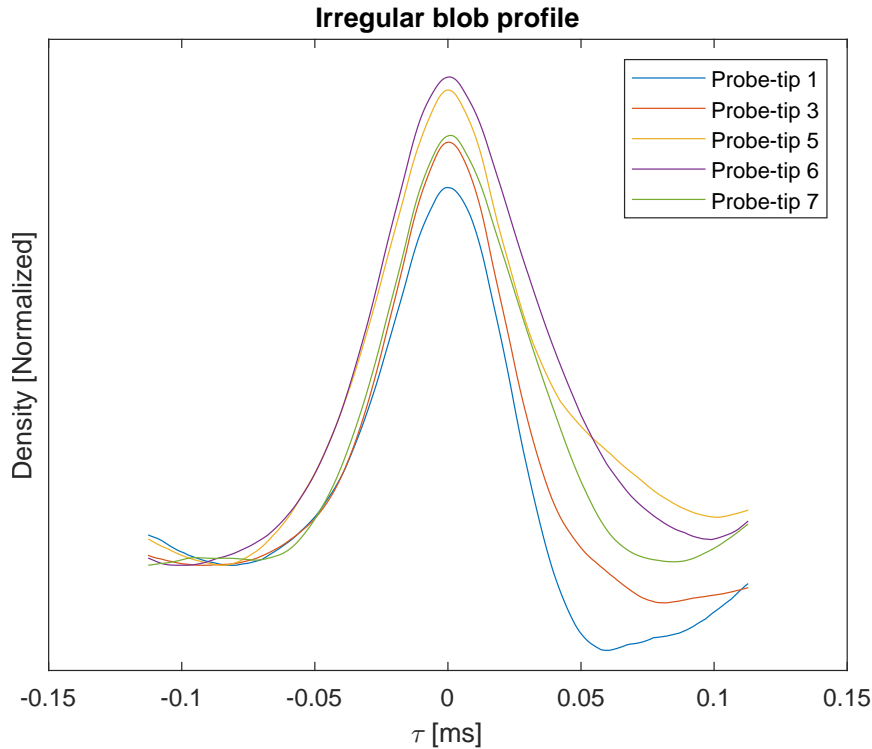
Figure 5.1: Normalised average of all irregular blobs detected in NORTH.

have a somewhat similar shape to the blobs in the paper mentioned above, with a sharp rise and a slower descent. The difference between the shape of the irregular blobs and these might be due to the low sample rate when measuring the ion saturation current, as the blobs often only had very few data points. This, together with the uncertainty of finding the peaks of the blobs, might result in the gaussian shape due to the central limit theorem. Better diagnostics would be required to determine whether the shape of these blobs is gaussian or another shape. It wasn't taken into consideration that different blobs were propagating at different speeds at different probes, so the probes have measured the blobs to varying lengths of time since the blobs travel through some of the probes faster than others, which would also lead to increased uncertainties.

As seen in figure 4.27, the periodic blobs get thinner in cross-section the further it travels, while the irregular blobs widen. One explanation of why the blobs behave differently in this regard can be found in the simulation seen in appendix D. Here it is seen that depending on where the probe is located vertically compared to the blob, it might get broader or thinner as it travels outwards. The irregular and periodic blobs may be part of the same blob generation scheme. Still, depending on the relative height between the probe array and the generation of blobs, they might be measured as one
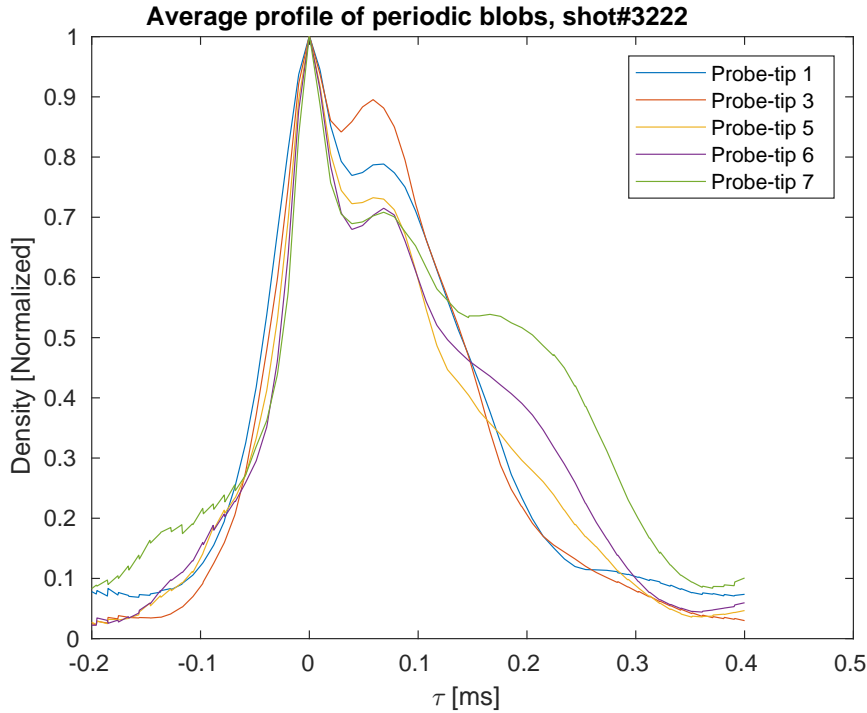
Figure 5.2: Normalised average of periodic blobs detected in NORTH shot#3222.

or the other type. To investigate whether this is possible, having probes in directions other than just a straight line would be beneficial.

During shots with both the old probe and the Lpa, modes, as seen in the top of figure 4.25, could be seen in the plasma. How these modes are made and why these blobs are detected at a close to constant frequency during the shots aren't clear. One hypothesis is that the plasma has increased confinement during these shots, meaning the density in the centre of the plasma is larger. If this plasma is over-dense, the O-wave heating can reflect off the plasma and instead heat the plasma at other positions than the centre of the plasma. This leads to the density of the plasma centre falling, which leads to the O-waves being able to heat the plasma again, leading to higher densities. This cycle of lower and higher densities could be measured as the periodic blobs we see. The fact that periodic blobs were more often generated when a vertical magnetic field was added supports this hypothesis, as the vertical magnetic field increases the confinement of the plasma.

To investigate this further, it would be advantageous if a 2-dimensional probe array were constructed to measure what happens in the plasma above/below $z = 0cm$ to determine whether it is heated/generated at those positions.

With the densities measured for the Lpa and the single probe, it can't be determined if OXB heating is happening in the tokamak, as the density

measured isn't higher than the $7.4 \times 10^{16} m^{-3}$ calculated density for over-dense plasma. Many of the densities measured are close to this barrier, so the plasma may be over-dense if the collection areas of the probes are larger than expected. Further experiments would have to take place to determine this. Since there haven't been any measurements with $r < 19cm$, the density may be larger further in the plasma, but it seems unlikely since the resonance heating happens at $r = 22cm$.

Given these results, it would be interesting to compare simulated plasma to these results and try and figure out which models best describe the NORTH tokamak to further assist in future research in plasma and tokamak physics.

Chapter 6

Conclusion

In this thesis, I have constructed a probe consisting of multiple Langmuir probes. This probe can simultaneously measure the plasma's density, temperature and floating potential in the tokamak NORTH at multiple positions. I have created and tested an amplifier setup for each Langmuir probe used in the probe, making it possible to measure the probes' signal without biasing the data acquisition system at the same large voltage as the probe. The probe has been used to experimentally show that radial plasma transport exists in the NORTH tokamak for plasma made with helium or hydrogen. This transport is found to be happening in 2 different regimes. In one case, irregular fast-moving blobs are generated at seemingly random times. These irregular blobs have a gaussian density profile, which gets wider the further out of the tokamak the blob travels. While in the second case, periodic blobs are generated at a close to constant interval. These blobs travel radially outwards slower than irregular blobs and get thinner the further they travel.

These results can be used to improve simulation tools and models for plasma and tokamak physics and thereby help further research, such as the ITER project, to obtain green energy from fusion sources earlier.

Appendix A
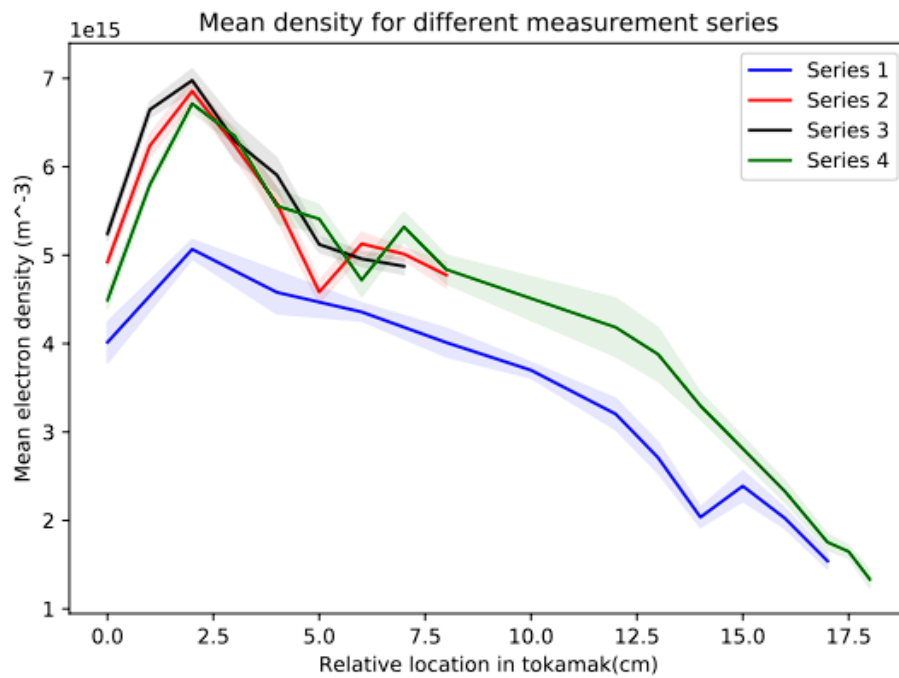
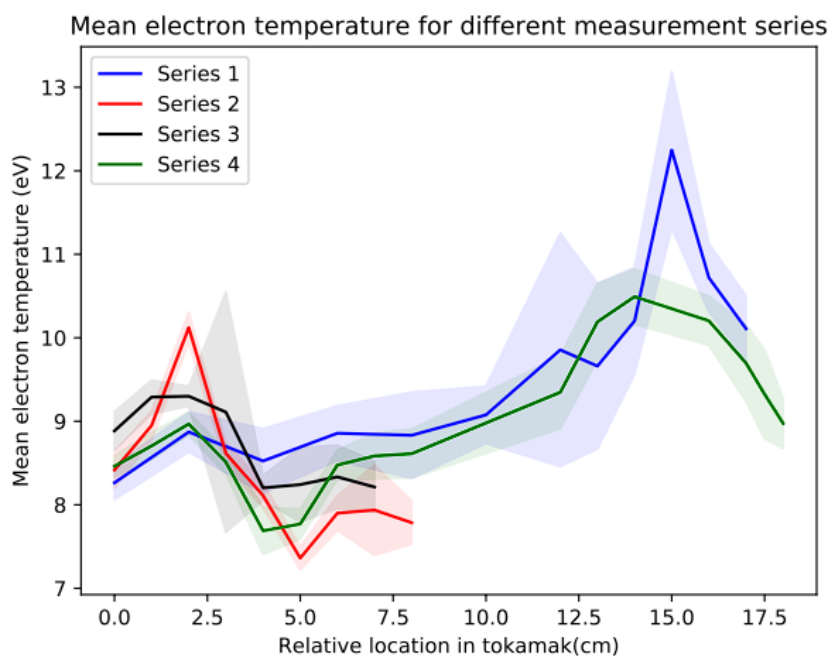(a) Mean electron density during shots versus relative probe location for different series.

Figure 3.3: Mean electron temperatures for 4 different measurement series where series 1 is taken several apart from the rest. Note that the measurement for series 4 at $R_{re} = 15$ cm is missing. The discrepancy that seems to be present should therefore be disregarded since we would most likely measure a large temperature for the series here as well.
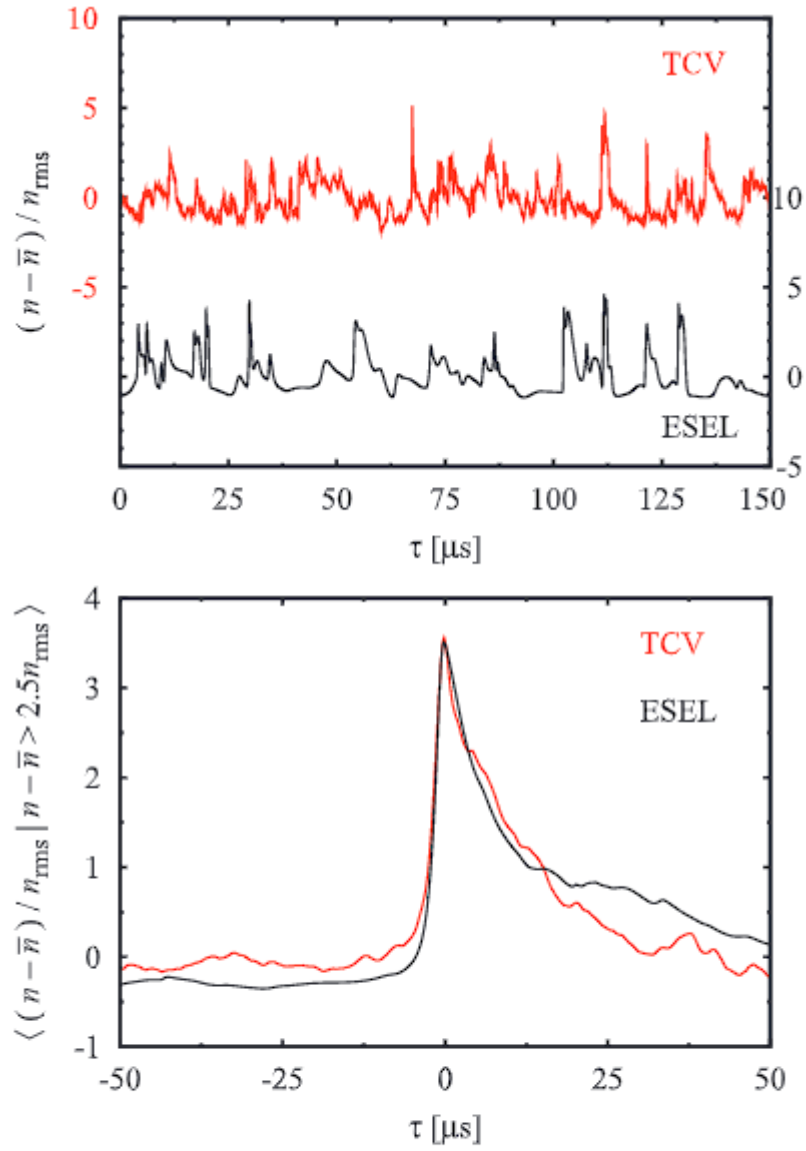
Appendix B

Fig. 4 Probe recording (top) of the particle density and its conditional average (bottom) in the TCV scrape-off layer and in a two-dimensional interchange turbulence simulation (ESEL).
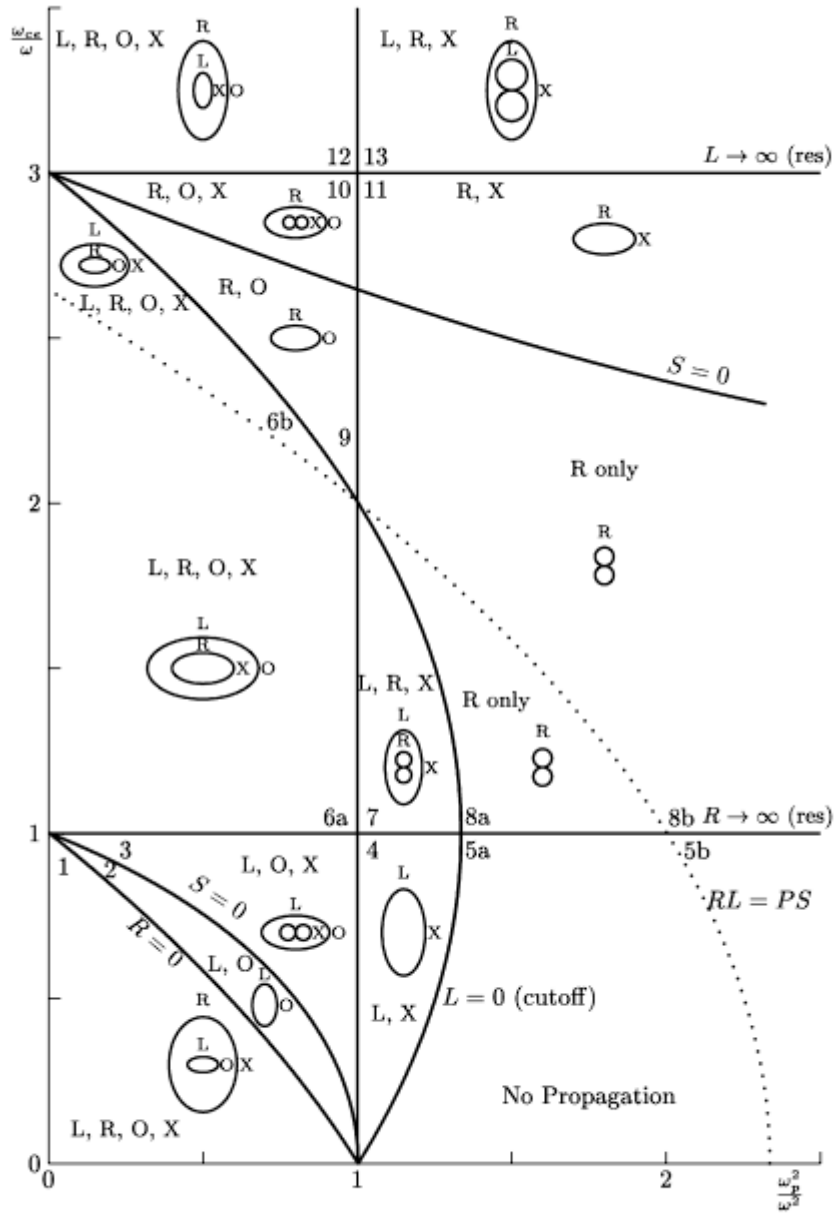
Appendix C

Figure 2.8. CMA diagram with all boundaries and wave normal surfaces (to scale with $m_i/m_e = 3$).

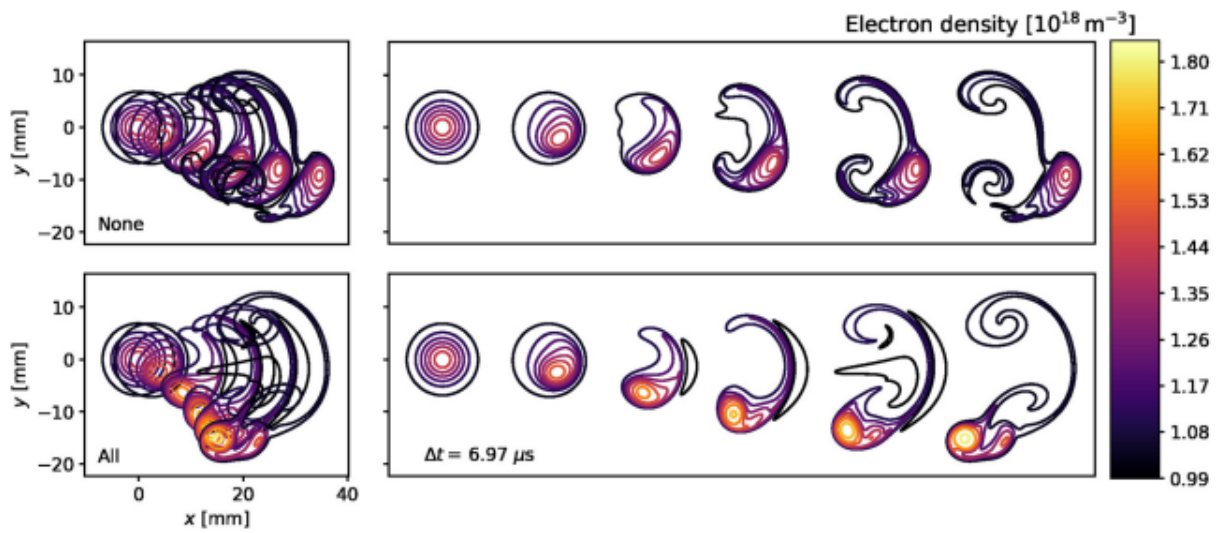Figure C.1: CMA diagram from *Plasma waves* by D. G. Swanson[17]

Appendix D

FIG. 1. Evolution of a seeded blob in a time span of 34.85 μs. The upper left frame shows the evolution without the influence of neutral interactions, and the lower left frame is with neutral interactions. In the right column of the frames, the snapshots are displaced horizontally for better visualization.

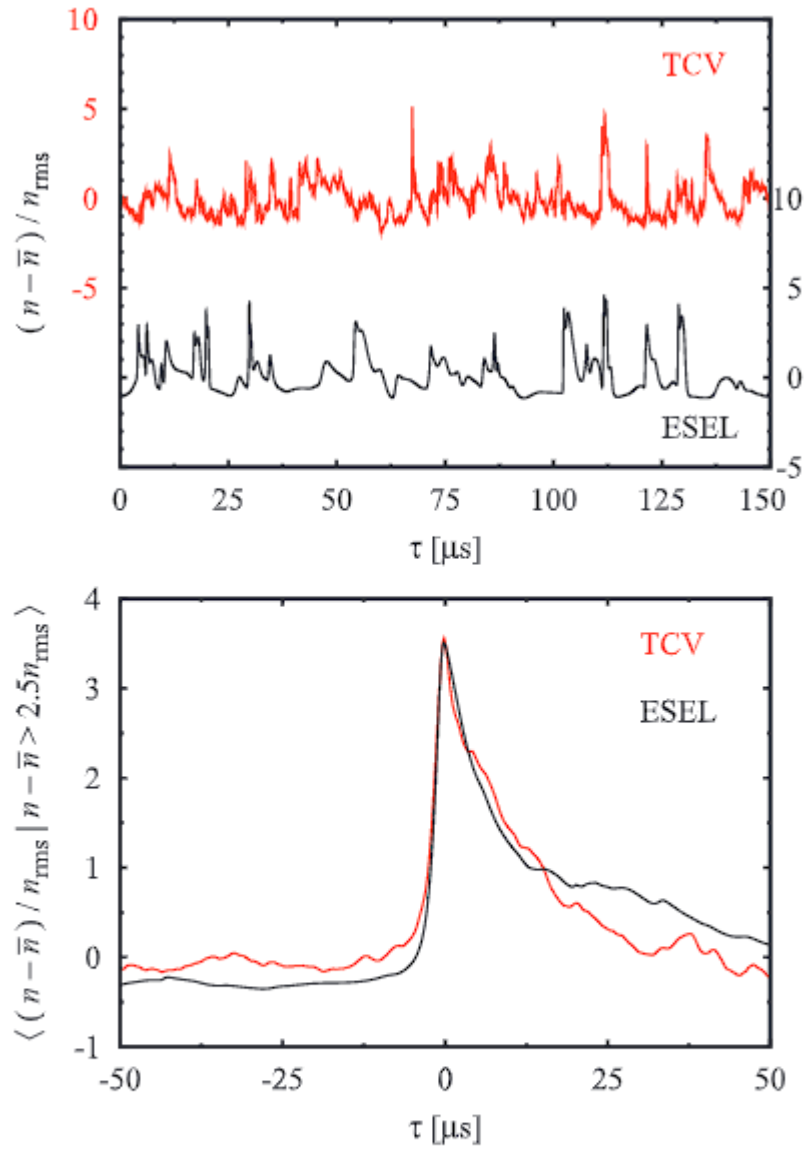Figure D.1: Simulation of seeded blobs done by A. E. Thrysøe[18]

Fig. 4 Probe recording (top) of the particle density and its conditional average (bottom) in the TCV scrape-off layer and in a two-dimensional interchange turbulence simulation (ESEL).

Figure D.2: Simulation and experimental data of blobs from ESEL[15] and TCV[6] respectively. Figure is made by [7]

.

Bibliography

[1] M. Baquero-Ruiz et al. "Dual Langmuir-probe array for 3D plasma studies in TORPEX". In: *Review of Scientific Instruments* 87.11 (Nov. 2016), p. 113504. ISSN: 0034-6748. DOI: 10.1063/1.4968024. URL: https://aip.scitation.org/doi/abs/10.1063/1.4968024.

[2] Ansgar Belke, Frauke Dobnik, and Christian Dreger. "Energy consumption and economic growth: New insights into the cointegration relationship". In: *Energy Economics* 33.5 (Sept. 2011), pp. 782–789. ISSN: 01409883. DOI: 10.1016/J.ENECO.2011.02.005.

[3] Francis F. Chen. "Introduction to Plasma Physics and Controlled Fusion". In: *Introduction to Plasma Physics and Controlled Fusion* (2016). DOI: 10.1007/978-3-319-22309-4.

[4] Steven Chu and Arun Majumdar. "Opportunities and challenges for a sustainable energy future". In: *Nature 2012 488:7411* 488.7411 (Aug. 2012), pp. 294–303. ISSN: 1476-4687. DOI: 10.1038/nature11475. URL: https://www.nature.com/articles/nature11475.

[5] *Fusion Conditions - EUROfusion.* URL: https://euro-fusion.org/fusion/fusion-conditions/.

[6] *Fusion Plasmas – TCV tokamak – SPC - EPFL.* URL: https://www.epfl.ch/research/domains/swiss-plasma-center/research/tcv/.

[7] O E Garcia. "Blob Transport in the Plasma Edge: a Review *)". In: *Plasma and Fusion Research: Review Articles* 4 (2009), p. 19. DOI: 10.1585/pfr.4.019.

[8] Paul Horowitz and Winfield Hill. "THE ART OF ELECTRONICS Third Edition". In: (2015). URL: www.cambridge.org.

[9] *ITER - the way to new energy.* URL: https://www.iter.org/.

[10] R Kube and O E Garcia. "Velocity scaling for filament motion in scrape-off layer plasmas". In: (2011). DOI: 10.1063/1.3647553. URL: http://php.aip.org/php/copyright.jsp.

[11] Heinrich Peter Laqua. "Electron Bernstein wave heating and diagnostic". In: *Plasma Physics and Controlled Fusion* 49.4 (Mar. 2007), R1. ISSN: 0741-3335. DOI: 10.1088/0741-3335/49/4/R01. URL: https://iopscience.iop.org/article/10.1088/0741-3335/49/4/R01https://iopscience.iop.org/article/10.1088/0741-3335/49/4/R01/meta.

[12] Robert L. Merlino. "Understanding Langmuir probe current-voltage characteristics". In: *American Journal of Physics* 75.12 (Nov. 2007), p. 1078. ISSN: 0002-9505. DOI: 10.1119/1.2772282. URL: https://aapt.scitation.org/doi/abs/10.1119/1.2772282.

[13] Bv H M Mott-Smith and Irving Langmuir. "OCTOBER) 1926 PHYSICAL REVIEW VOLUME 28' THE THEORY OF COLLECTORS IN GASEOUS DISCHARGES". In: ().

[14] S. K. Nielsen et al. "First results from the NORTH tokamak". In: *Fusion Engineering and Design* 166 (May 2021). ISSN: 09203796. DOI: 10.1016/J.FUSENGDES.2021.112288.

[15] Peter ; Ondac et al. "Comparison between 2D turbulence model ESEL and experimental data from AUG and COMPASS tokamaks". In: *Acta Polytechnica* 55.2 (2015), pp. 128–135. ISSN: 1210-2709. DOI: 10.14311/AP.2015.55.0128. URL: https://orbit.dtu.dk/en/publications/comparison-between-2d-turbulence-model-esel-and-experimental-data.

[16] K. U. Riemann. "The Bohm criterion and sheath formation". In: *Journal of Physics D: Applied Physics* 24.4 (Apr. 1991), p. 493. ISSN: 0022-3727. DOI: 10.1088/0022-3727/24/4/001. URL: https://iopscience.iop.org/article/10.1088/0022-3727/24/4/001https://iopscience.iop.org/article/10.1088/0022-3727/24/4/001/meta.

[17] D Gary Swanson. "Series in Plasma Physics Plasma Waves, 2nd Edition". In: (2003).

[18] AS Thrysøe et al. "Dynamics of seeded blobs under the influence of inelastic neutral interactions". In: *aip.scitation.org* 26.5 (May 2020), p. 2023. DOI: 10.1063/5.0003262. URL: https://aip.scitation.org/doi/abs/10.1063/5.0003262.

[19] *What is LabVIEW? Graphical Programming for Test & Measurement - NI*. URL: https://www.ni.com/da-dk/shop/labview.html.